



# 1 The patchwork loess of Central Asia: Implications for interpreting aeolian 2 dynamics and past climate circulation in piedmont regions

3 Aditi K. Dave<sup>1,2†</sup>, Lenka Lisá<sup>3</sup>, Giancarlo Scardia<sup>4</sup>, Saida Nigmatova<sup>5</sup>, Kathryn E. Fitzsimmons<sup>1,2</sup>

4 <sup>1</sup>*Research Group for Terrestrial Palaeoclimates, Max Planck Institute for Chemistry, Mainz,*  
5 *Germany*

6 <sup>2</sup>*Department of Geosciences, University of Tübingen, Schnarrenbergstrasse 94-96, 72076*  
7 *Tübingen*

8 <sup>3</sup>*Institute of Geology, Czech Academy of Sciences, Prague, Czech Republic*

9 <sup>4</sup>*Instituto de Geociências e Ciências Exatas, Universidade Estadual Paulista (UNESP), 13506-900*  
10 *Rio Claro SP, Brazil*

11 <sup>5</sup>*Institute of Geological Sciences K. Satpaeva, Ministry for Education and Science of the Republic*  
12 *of Kazakhstan, Almaty, Kazakhstan*

13 <sup>†</sup>present address

14

15 Corresponding author: Aditi K. Dave; email – aditikrishna.dave@gmail.com

16

## 17 ABSTRACT

18 Reconstruction of mass accumulation rates (MARs) in loess deposits are widely used for  
19 interpreting long-term aeolian transport and climate dynamics in terrestrial environments.  
20 However, these interpretations are often driven by preponderance of reconstructions from  
21 individual or selected sites, which can bias our understanding of past climate, especially in the  
22 absence of other proxy information. Recent studies on MARs from multiple loess sites in Arid  
23 Central Asia (ACA) reveal disparities in the timing of peaks in accumulation between sites, as  
24 well as asynchronies with loess flux in the Chinese Loess Plateau (CLP). We investigate this issue  
25 by (1) dating five new sites from the western Ili Basin, therefore extending the spatial cover of  
26 loess chronologies across ACA and (2) combining that with MARs from >30 sites across ACA  
27 and the CLP over the last 60 ka. Our results indicate spatio-temporal inhomogeneity in the  
28 timing and rate of loess deposition across the ACA, and highlight the importance of  
29 interrogating local and regional influences on dust supply and transport. Our synthesis of  
30 MAR's from ACA and CLP suggests that the timing of peak dust flux as an indicator of large-  
31 scale climate dynamics is best derived from an aggregate of sites; this removes site-specific  
32 bias where local processes or topographic setting outweigh the climate signature.

33

## 34 Keywords:

35 Loess, Luminescence dating, Mass accumulation rates, Central Asia, Chinese loess Plateau

36

37



## 38 INTRODUCTION

39 Dust is an important constituent of the climate system. It can act as a trigger for climate  
40 change, whether directly by altering the radiative balance of the Earth, or indirectly by  
41 changing the optical properties of clouds (Arimoto et al., 2001; Andrea and Rosenfeld, 2008).  
42 Iron in mineral dust acts as a limiting nutrient in oceans, increasing ocean productivity and  
43 thereby atmospheric greenhouse gas concentrations, thus acting as an additional indirect  
44 driver of climate change (Martin, 1990; Martinez-Garcia et al., 2014). Conversely, the  
45 production, transport and deposition of dust reflects an earth-surface response to climatic  
46 conditions. Consequently, deposits of wind-blown dust, known as loess (Pye, 1987; Pecs, 1990),  
47 are recognised as significant terrestrial archives of past climate change (Liu, 1985;  
48 Smalley et al., 1995, 2005; Muhs, 2007), especially in the semi-arid and sub-humid temperate  
49 latitudes (Fitzsimmons, 2017).

50 Reconstruction of changes in loess accumulation rates is one of the most commonly used  
51 parameters for inferring past climatic conditions and atmospheric dust load. The quantification  
52 of loess sedimentation as mass accumulation rates (MARs) not only facilitates direct  
53 comparison between different sites, but also the reconstruction of large-scale dust flux  
54 patterns over glacial-interglacial timescales (Kohfeld and Harrison, 2003). In addition, loess  
55 MAR datasets provide input to models to better understand the role of dust feedback  
56 mechanisms within the climate system (Albani and Mahowald, 2019; Schaffernicht et al.,  
57 2020). On this basis, it is essential to ensure that interpretation of MAR datasets reflects a  
58 robust understanding of the various geological and climatic factors affecting loess  
59 accumulation rates in a given region.

60 Loess MAR's as a gauge for palaeoenvironmental conditions is based on the widespread  
61 assumption that loess accumulation increases during drier, colder and/or windier climate  
62 phases, and decreases and is overprinted by soil development during wetter, warmer and/or  
63 less windy periods. It is this hypothesis on which correlations between loess profiles are  
64 overwhelmingly predicated, both within (e.g., Kukla et al., 1988; Kohfeld and Harrison, 2003;  
65 Sun and An, 2005; Fitzsimmons et al., 2012) and between regions (Markovic et al., 2015).  
66 Calculations of loess accumulation are mostly based on luminescence dating, which  
67 determines the timing of burial of ubiquitous quartz and feldspar minerals and which, having  
68 a higher upper dating limit than radiocarbon, can therefore extend the chronological length of  
69 the quantitative record (Singhvi et al., 2001; Stevens, 2019). Recently, an increase in studies  
70 applying high-resolution luminescence dating to loess deposits has started to suggest a lack of  
71 uniformity in accumulation rates (Ujvari et al., 2010; Fitzsimmons et al., 2017), even at  
72 individual sites (e.g., Fitzsimmons and Hambach, 2014; Sprafke et al., 2018; Stevens et al., 2018;  
73 Fenn et al., 2020). These results call into question the presumed primary association between  
74 loess accumulation and climatic controls, and prompt a reconsideration of geological controls  
75 on aeolian flux.



76 Central Asia (hereafter Arid Central Asia or ACA), defined here as the region to the north of the  
77 Asian high mountains and between the Caspian Sea and Mongolia, is an arid region at the  
78 intersection between two major Northern hemisphere climate systems, the mid-latitude  
79 Westerlies and the Siberian High. ACA is assumed to be a major contributor to the global dust  
80 cycle (Narsima, 2007; Kok et al., 2021), based on both its climatic context and widespread thick  
81 loess deposits. The region therefore represents an invaluable natural laboratory for exploring  
82 loess accumulation as a response to climate. Recently produced chronological datasets from  
83 loess sites in ACA (Li et al., 2016a, 2018a; Fitzsimmons et al., 2018) indicate a high degree of  
84 variability in the timing and peak of loess accumulation between sites, therefore challenging  
85 prevailing assumptions linking aeolian flux to cold, dry phases, and with the timescales of  
86 glacial-interglacial climate variability. It has since been suggested, on the basis of modelled dust  
87 trajectories, that the topographic complexity and diverse landscape features (desert dunes,  
88 stony pavements, alluvial deposits and floodplains) in ACA lead to a complex interaction  
89 between topography, wind dynamics, sediment availability and supply (Fitzsimmons et al.,  
90 2020). We therefore expect that it is not just climate that plays a major role in dictating the  
91 pattern and distribution of loess flux in this region and possibly elsewhere, but that other  
92 factors must be taken into equal consideration.

93 In this study, we investigate spatial variability in timing and rates of loess accumulation across  
94 the Ili Basin of southeast (SE) Kazakhstan, and in ACA more widely. We undertake a two-fold  
95 approach. Firstly, we obtain a high-resolution chronological record based on luminescence  
96 dating for five loess sites in the as-yet understudied central and western part of the Ili Basin;  
97 providing an additional 200 km of spatial coverage to the loess record in the region. We  
98 integrate our new chronologies with published luminescence dated loess records from eastern  
99 part of the basin to derive a conceptual understanding of aeolian dynamics within the Ili Basin  
100 with respect to timing and topography. Secondly, we calculate MARs for all reliably dated Ili  
101 Basin loess sites, as well as for additional sites across ACA and the Chinese Loess Plateau (CLP),  
102 to synthesise the spatial distribution of dust flux and the timing of peak accumulation with  
103 respect to geographic setting and larger scale climate drivers across Central and East Asia.

104

## 105 REGIONAL SETTING

106 Arid Central Asia (ACA) is a predominantly arid to semi-arid region, defined here as extending  
107 from the Caspian Sea in the west to the Mongolian Hangay uplands in the east (Schäetzl et al.,  
108 2018). ACA forms a wide belt in the rain shadow north of the Asian high mountains, including  
109 the actively uplifting Pamir, Alai and Tien Shan (Schurr et al 2014; Grützner et al., 2017). The  
110 region features loess-draped piedmonts, alluvial fans, dune fields, and the large endorheic  
111 basins of the Aral Sea and Lake Balkhash. ACA experiences an extremely continental, semi-arid  
112 climate. Its present-day climate is driven by the interaction between two main climatic features  
113 – the mid-latitude Westerlies and the high-altitude polar front, linked to the Siberian High  
114 Pressure system, from the north. Seasonal variations in wind direction and precipitation are



115 strongly influenced by the interaction between these subsystems and the orography of the  
116 region (Lydolph, 1977; Machalett et al., 2008).

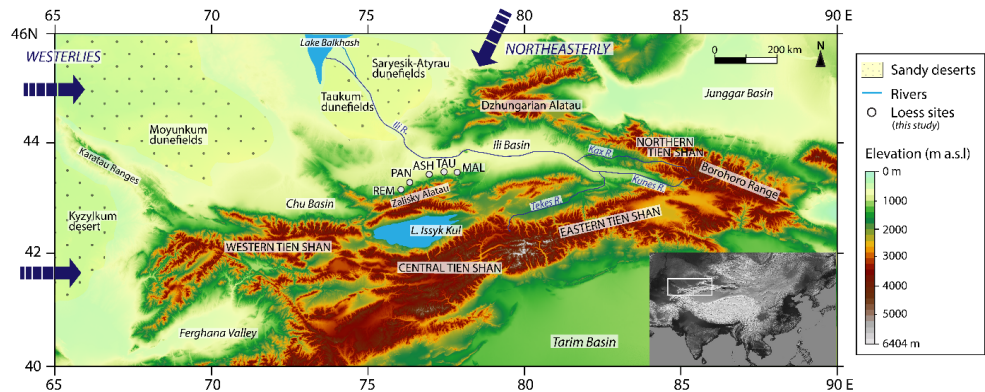
117 This study focuses on the loess deposits that drape the piedmonts of the central and eastern  
118 Tien Shan mountain ranges within the Ili Basin, located in SE Kazakhstan and northwest China.  
119 The Ili River (also referred to as Yili, Fig. 1) is the main inflow of Lake Balkhash; its main  
120 tributaries include the Kashi, Tekes and Kunes Rivers, which originate in the upper, Chinese  
121 part of the basin. The Ili Basin is surrounded by the Tien Shan mountain ranges to the south,  
122 the Chinese Borohoro range to the east, and the Dzhungarian Alatau and northern Tien Shan  
123 to the northeast, forming a funnel shape that opens to the west, exposing it to the prevailing  
124 westerly and northerly winds and the associated dust transport pathways believed to facilitate  
125 loess accumulation along the piedmonts. The basin opens out at the “Ili Gate” onto the alluvial  
126 fans, plains and dunefields of the “Ili plain”.

127 The source of loess in the Ili Basin and along the Tien Shan piedmont of the Ili plain is still  
128 unclear. Early models (e.g., Obruchev, 1945) posit that the dune fields of the Ili plain to the  
129 north, including the Saryesik-Atyrau and Taukum (Fig. 1), act both as sediment sinks for  
130 material transported from the Tien Shan, and as sources for dust entrainment and transport  
131 back onto the piedmont. Recent investigations based on loess bulk chemistry and grain-size  
132 from the eastern, Chinese side of the Ili Basin (Li et al., 2018b) suggest that the loess is  
133 predominantly locally sourced, with distal, desert-derived material increasing in contribution  
134 westward along the piedmont. Models for fine-grained sediment transport suggest that both  
135 local and distal transport, as well as the funnelling or obstructing effect of topography, play a  
136 role (Fitzsimmons et al., 2020). The setting of individual sites with respect to topography and  
137 sediment transport would therefore likely influence the degree to which loess sediments  
138 accumulate and preserve responses to past climatic conditions.

139 Loess deposits in the Ili catchment vary substantially in thickness, from more than 100 m (Song  
140 et al., 2014) to less than 1 metre. The distribution and thickness of loess in the eastern  
141 (Chinese) part of the Ili Basin was described by Song et al. (2014); as yet there is minimal data  
142 available for the western and central (Kazakh) part of the basin. Likewise, in the past decade,  
143 a number of high-resolution dated loess records have been published from the eastern,  
144 Chinese, part of the Ili basin (E et al., 2012; Song et al., 2012, 2015; Kang et al., 2015; Li et al.,  
145 2018a, 2020a; Wang et al., 2019a,b; Yang et al., 2020), while the central, Kazakh part of the  
146 basin remains largely unexplored. Field observations along the Kazakh Ili piedmonts in 2015  
147 (Sprafke et al., 2018) and again in 2017 suggest that loess deposits here, in contrast to the  
148 Chinese Ili (Song et al., 2014) are discontinuous, highly variable in thickness and are distributed  
149 along the mountain foothills, infilling valleys and draping alluvial plains along the range front.  
150 Here we investigate five loess sections from a c. 200 km east-west (E-W) transect along the  
151 Tien Shan piedmont within the Ili catchment, extending from the enclosed part of the basin,  
152 through the Ili Gate and onto the Ili plain (Fig. 1).



153



154

155 Fig. 1. Regional setting and location of loess sites under study. The elevation map was made  
156 using open source Shuttle Radar Topography Mission (SRTM) data provided by AW3D of the  
157 Japan Aerospace Agency.

158

159

## 160 MATERIAL AND METHODS

### 161 Field work and Site description

162 We sampled five loess sections from a c. 200 km E-W transect along the Zhalysky Alatau range  
163 front in SE Kazakhstan (Fig. S1). Since all sites were exposed as vertical cliff sections, we  
164 undertook fieldwork by abseil to ensure continuous down-profile observations and sampling.  
165 Prior to sampling, we cleared back at least 50 cm of the surface sediment to prevent  
166 contamination by recent sediment relocation and to expose undisturbed sections. A brief  
167 description of our site locations is given below.

168 *Remizovka* (hereafter REM, 43° 13.2' N, 76° 51' E; 1070 m a.s.l.) is a >25 m-thick section  
169 exposed on a hillslope, originally excavated for the construction of ski jump facilities on the  
170 southern margins of Almaty city. Loess at the site has previously been described and dated by  
171 luminescence (Machalett et al., 2006, 2008; Fitzsimmons et al., 2018; Sprafke et al., 2018). A  
172 radiocarbon-dated subsection, which has since been removed during road construction  
173 (referred to as Trampolin, Feng et al., 2011), was recently placed in stratigraphic context to  
174 clarify ambiguity between studies (Sprafke et al., 2018). Our study here focusses on the  
175 uppermost 7 m of the main section.

176 *Panfilov* (PAN, 43° 22.295' N, 77° 07.670' E; 710 m a.s.l.), is a c. 5 m thick site located just  
177 southwest of the village of Panfilovo, c. 40 km northeast of Almaty. The loess section has been  
178 exposed as a result of erosion by the Tsyganski Creek, which flows northward from the Tien  
179 Shan.



180 *Ashubulak* (ASH, 43° 28.671' N, 77° 47.379' E; 760 m a.s.l.) is located at the southern edge of  
181 the village of the same name, c. 50 km east of the PAN section. The exposed outcrop at this  
182 site is 5.1 m-thick and is entirely composed of pale yellowish primary loess. Like PAN, the ASH  
183 site is also located along the peripheral edge of the piedmont loess, where the loess deposits  
184 taper out northwards onto alluvial fans.

185 *Taukaraturyk* (TAU, 43° 29.445' N, 78° 01.509' E; 769 m a.s.l.), is a 7.5 m-thick profile located  
186 on the southern edge of the village of Taukaraturyk, c. 20 km and c. 100 Km east of ASH and  
187 Almaty respectively. Unlike the loess-marginal sites of PAN and ASH, which are located in more  
188 open, exposed sections c. 10 km out from the range front, the TAU site is located much closer  
189 to the mountain ranges (c. 1 km north of the first ridge of the Zhalysy Alatau).

190 *Malubai* (MAL, 43° 26.312' N, 78° 19.763' E; 815 m a.s.l.), is located c. 20 km south of the city  
191 of Chilik (Shelek) and c. 25 km east of TAU. The exposed outcrop at MAL is 6 m-thick, and lies  
192 on the northern slope of a northeast-southwest bifurcating flank of the Zhalysy Alatau, and is  
193 consequently more sheltered than the other sites.

194

## 195 Proxy indices

196 Samples for micromorphology, grain-size analyses and magnetic susceptibility were collected  
197 from four sites (PAN, ASH, TAU and MAL) at 10 cm intervals. We collected these samples in 8  
198 cm<sup>3</sup> plastic boxes hammered into the cleaned-back profiles. The same sample material was  
199 used for all three analyses in the order described below. Grain size and magnetic susceptibility  
200 data for the site of REM was already available from previous work (Fitzsimmons et al, 2018;  
201 Schulte et al., 2018).

### 202 Magnetic susceptibility

203 Magnetic susceptibility measurements were performed on 228 samples from four sites (PAN,  
204 ASH, TAU, MAL) using AGICO Kappabridge MFK2 at the Alpine Palaeomagnetism Laboratory  
205 (Peveragno, Italy). The samples were air dried at 50 °C and measured at room temperature  
206 with an alternating current magnetic field with an amplitude of 20 A/m at 976 Hz (low  
207 frequency). The low frequency measurements were repeated two times for each sample; the  
208 mean was taken for the final calculation of normalised mass-specific bulk magnetic  
209 susceptibility ( $\chi_m$ ).

### 210 Micromorphology

211 Eighteen selected samples were prepared for micromorphological analysis from three loess  
212 localities (PAN, ASH and TAU). The samples were impregnated in vacuum chamber using  
213 PolyLite 2000 and after curing, the thin sections were observed using a polarising microscope  
214 at resolution ranges of 16-800x at the Institute of Geology, Czech Academy of Sciences



215 (Prague). The micromorphological descriptions follow Stoops (2003) and are summarised in  
216 Table S1 of the Supplementary information (SI)

### 217 *Grain size*

218 Grain-size analyses were undertaken on 228 samples from four sites (PAN, ASH, TAU and MAL)  
219 following two different preparation methods: the total dispersion method (Konert and  
220 Vandenberghe, 1997) and dispersion in KOH (Łomotowski et al., 2008). For the total dispersion  
221 method, samples were dispersed in 10% KOH solution and then treated with HCl and H<sub>2</sub>O<sub>2</sub> to  
222 remove carbonates and organic matter respectively. The KOH dispersion method involved  
223 measurement following sediment dispersion in 10% KOH solution. All grain-size measurements  
224 were undertaken at the Institute of Geology at the Czech Academy of Sciences, Prague, using  
225 a CILAS 1190 LD laser particle analyser, with a measurement range of 0.04–2000 µm and  
226 analytical error of <2 %. We evaluated mean grain size using the GRADISTAT program (Blott  
227 and Pye, 2001). Sedimentology and wind-strength interpretations were made on the basis of  
228 mean grain size, the proportion of ≤ 4 µm grains (determined using both preparation methods),  
229 as well as the grain size index (GSI: %26–52 µm / %<26 µm; Antoine et al., 2009; based on the  
230 total dispersion method).

### 231 **Luminescence dating**

232 Samples for luminescence dating were collected at 1 m intervals from all five profiles (REM,  
233 PAN, ASH, TAU and MAL) by hammering 3.5 cm-diameter, 10 cm-long steel tubes into freshly  
234 cleaned loess sections. A total of 27 samples were collected from five sites. Additional sediment  
235 for dose-rate analysis was collected from the material immediately surrounding the tubes. The  
236 exposed outer material from the ends of the steel tubes was used for determining water  
237 content; sediment from the inner parts of the tubes was processed for equivalent dose  
238 analysis. All samples were processed under subdued red-light conditions at the Institute of  
239 Geosciences, Johannes Gutenberg University, and measured at the Max Planck Institute for  
240 Chemistry, respectively (Mainz, Germany). Wet sieving of sediment yielded insufficient coarse  
241 grains (>63 µm) for measurement; we therefore prepared fine-grained (4–11 µm) quartz and  
242 polymineral samples using established protocols (Frechen et al., 1996; Timar-Gabor et al.,  
243 2010).

244 We measured equivalent dose ( $D_e$ ) using optically stimulated luminescence (OSL) based on the  
245 single aliquot regenerative dose (SAR) protocol (Murray and Wintle, 2000; 2003) for the quartz  
246 fraction, and elevated temperature post-infrared infrared stimulated luminescence (pIRIR;  
247 Thiel et al., 2011) for the polymineral fine-grained (K-feldspar-bearing) material. In order to  
248 negate the suspicion of any feldspar contamination of the OSL signal from the quartz-rich fine  
249 grains, we applied the double-SAR approach (DSAR, Banerjee et al 2001; Jain and Singhvi, 2005;  
250 Dave et al., 2018), which includes an additional IR stimulation prior to all blue stimulation steps  
251 within the SAR protocol. In samples where saturation of the quartz OSL signal was suspected





252 (after Timar-Gabor et al., 2017), elevated pIRIR signals from fine-grained polymineral samples  
253 was used for  $D_e$  determination.

254 Radionuclide concentrations for dose-rate determination were analysed using high-resolution  
255 germanium gamma spectrometry, measured at the Felsenkeller, VKTA Dresden. Dose rates  
256 were calculated from the radionuclide concentrations using published conversion factors  
257 (Guerin et al., 2011), combined with measured moisture content and published equations for  
258 cosmic-ray dose rate contributions (Prescott and Hutton, 1994). A detailed account of sample  
259 preparation, luminescence measurements and protocols, and dose-rate calculations can be  
260 found in the SI.

## 261 Age-depth modelling and mass accumulation rates

262

263 Based on our investigations of fine-grained quartz as discussed below and the reliability of  
264 quartz-based OSL ages, we limited our assessment of loess MARs to the past 60 ka. The  
265 presence of a substantial number of dated loess sites within this age range allows for a good  
266 representation of loess sedimentation patterns across the Ili Basin, elsewhere in ACA and  
267 across the CLP.

268 We undertook age-depth modelling and calculated sediment accumulation rates for 30  
269 additional sites based on published luminescence ages (based on quartz OSL and feldspar pIRIR  
270 ages) that span the time period 0-60 ka. Our analysis was based on high resolution  
271 luminescence ages taken from 14 sites across the Ili Basin (including sites from the present  
272 study), 8 sites from neighbouring sedimentary basins in ACA, and 11 representative sites from  
273 the CLP. Age-depth modelling for all sites was performed using the R package Bacon (Blaauw  
274 and Christen, 2011). The age-depth models derived using R-Bacon were used to estimate the  
275 corresponding sedimentation rates ( $SR$ ,  $\text{cm ka}^{-1}$ ), and then to evaluate MAR's ( $\text{g cm}^{-2}\text{ka}^{-1}$ ) using  
276 the equation:  $MAR = SR \times \rho_{\text{dry}} \times f_{\text{eol}}$ , where  $\rho_{\text{dry}}$  is the dry bulk density ( $\text{g cm}^{-3}$ ) and  $f_{\text{eol}}$  refers to  
277 the sediment fraction that is aeolian in nature (Kohfeld and Harrison, 2000). We used a value  
278 of  $f_{\text{eol}} = 1$  for all calculations, since we assume that loess is entirely aeolian in nature. Based on  
279 published literature, we utilised mean bulk density values of  $1.5 \text{ g cm}^{-3}$  for ACA (based on values  
280 obtained by Jia et al., 2018; Wang et al., 2019a; Li et al., 2019a) and  $1.48 \text{ g cm}^{-3}$  for sites in the  
281 CLP (Kohfeld and Harrison, 2003; Kang et al, 2015). Details of the sites analysed in this study  
282 (and the selection thereof), criteria for the selection of luminescence ages, age-depth model  
283 parameters for R-Bacon, the constraints for MAR calculations and subsequent interpretation  
284 of different sites (where relevant) are described in the SI.

285

## 286 RESULTS

### 287 Stratigraphy and sediment characteristics





288 The stratigraphy of our five investigated sections, including grain size and magnetic  
289 susceptibility can be seen in Fig. 2. A detailed account of the micromorphological  
290 characteristics are summarized in Table S1 of the SI.

291 We focused on the uppermost 7 m of the REM loess profile, which spans c. 35-15 ka (based on  
292 pIRIR<sub>290</sub> dating; Fitzsimmons et al., 2018). The top 0.8 m of this section is characterised by  
293 recent soil formation, including penetration by living plant roots. A carbonate-enriched  
294 subhorizon is observed at 0.8–1.5 m depth, below which massive, homogenous primary loess  
295 is observed down to 7.2 m. The magnetic susceptibility record shows relatively little variation  
296 down the profile below the recent soil. The grain-size record similarly yields minimal variations,  
297 with the exception of a slight increase in the coarser fraction at 3.9–4.3 m and 5.9–6.1 m  
298 depths (Schulte et al., 2018). Additional observations relating to colour indices and pedology  
299 are described in Fitzsimmons et al. (2018).

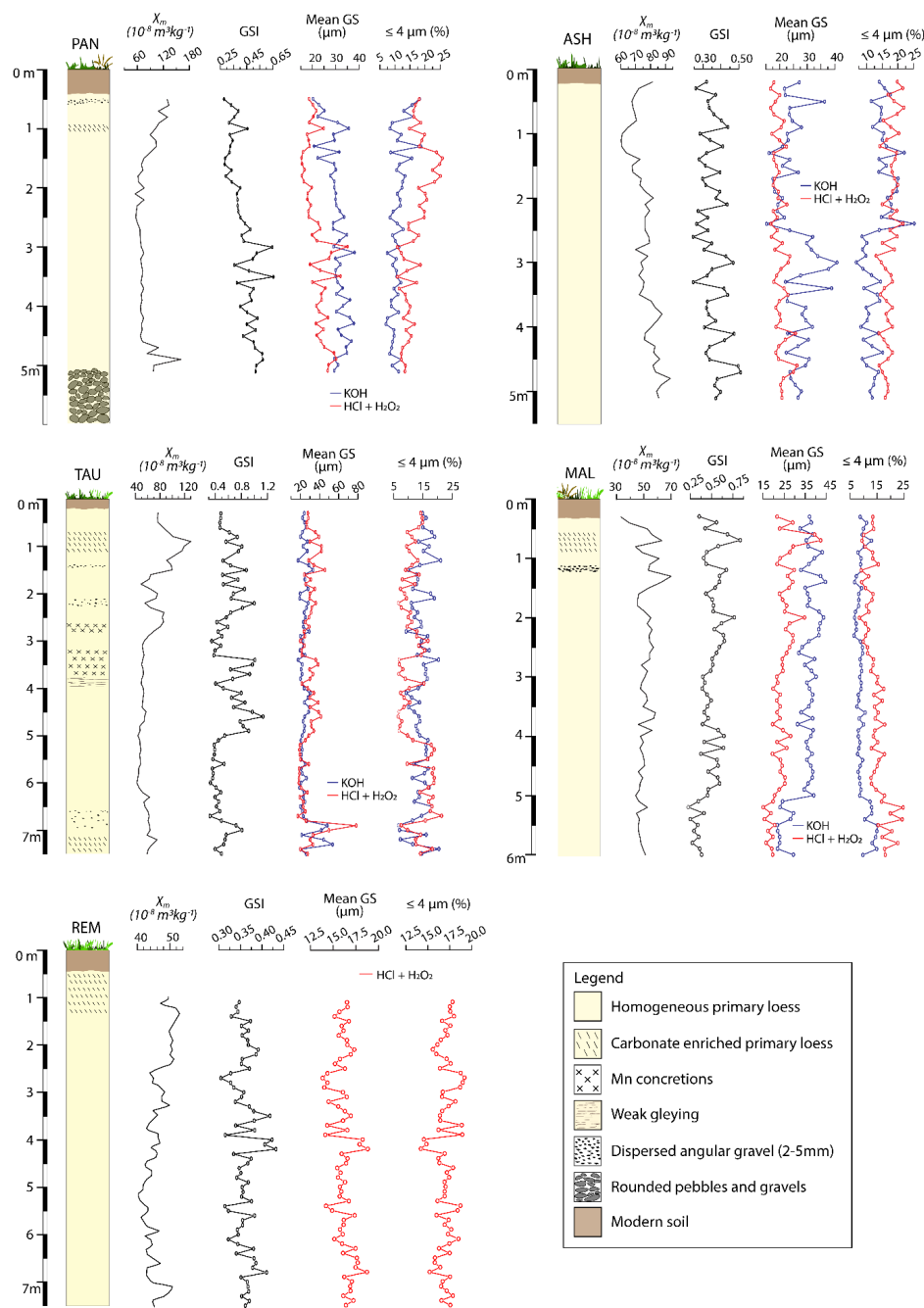
300 The PAN section is 5.1 m-thick and overlies a >3 m-thick fluvial gravel bed; the imbrication of  
301 cobbles indicates northward flow. The uppermost 0.5 m of the section comprises modern soil,  
302 penetrated by present-day roots. At 0.5–0.7 m, we observe a slightly darker humic horizon,  
303 which is intercalated with colluvial loess-like material. Below this layer and down to 0.9 m,  
304 colluvial angular clasts (2-4 mm) are observed which grade downwards into loess-like  
305 sediment. The upper c. 1.2 m yields higher magnetic susceptibility values (c.  $130\text{--}90 \times 10^{-8}$   
306  $\text{m}^3\text{kg}^{-1}$ ) that support our observations of weathering and soil formation. From c. 0.9–5.1 m, the  
307 section is composed of pale yellowish primary loess, with a carbonate-enriched layer at 0.9–  
308 1.2 m. Reduced magnetic susceptibility values (c.  $60 \times 10^{-8} \text{m}^3\text{kg}^{-1}$ ) below c. 1.2 m are consistent  
309 with un-weathered, primary loess deposits. Micromorphological analyses of 4 samples (Table  
310 S1) from the uppermost primary loess (0.9 to 2 m depth) shows dominant well sorted, fine-  
311 grained aeolian silt mixed with coarser, angular colluvial material (<4 mm); these observations  
312 are supported by the grain-size results (Fig. 2). The total dispersion method, which dissociates  
313 aggregates, yields a higher proportion of very fine clasts (<4  $\mu\text{m}$ ) than the KOH method, which  
314 indicates high proportion of aggregates from 0.5-2 m. The aggregates are most likely derived  
315 from a combination of colluvial clasts, disintegration of carbonate-coated or carbonate-rich  
316 clasts, and aggregation by organic matter present in the sediment. We observe an abrupt  
317 increase in magnetic susceptibility at the base of the loess just above the gravels, although the  
318 reason for this is unclear.

319 The outcrop at ASH is 5.1 m-thick and is entirely composed of pale yellowish primary loess. The  
320 modern soil is c. 30 cm-thick with modern rootlets. While the geographic situation of ASH is  
321 similar to PAN, located along the northern margin of the piedmont loess deposits, the ASH  
322 sediments are more consistent with homogenous, fine-grained primary loess and no colluvial  
323 input was observed. Magnetic susceptibility yields no major variations down the profile, which  
324 is consistent with primary loess deposition with no evidence of pedogenesis. Micromorphology  
325 of five selected samples (Table S1) provides further evidence of minimal disturbance of the  
326 sediments following aeolian deposition.



327 The TAU section is c. 7.5 m-thick. The uppermost 0.3 m is composed of a humic soil with  
328 modern rootlets and bioturbation, below which a blocky, carbonate-rich C horizon extends  
329 down to 0.7 m. From 0.7–7.5 m depth, the section comprises pale yellowish primary loess, with  
330 local occurrences of very coarse sand at depths of 1.5–2.0 m, 2.4–2.8 m, and 3.8–4.9 m.  
331 Carbonate mottling was observed at 1.8–2.9 m and 5.5–7.1 m, and minor manganese  
332 concretions occur at 2.4–2.8 m and 3.0–3.8 m. The magnetic susceptibility values show subtle  
333 variations along the profile. Higher values (c.  $90\text{--}120 \times 10^{-8} \text{ m}^3\text{kg}^{-1}$ ) occur in the uppermost 2.5  
334 m. We interpret these peaks as incipient pedogenesis which was not observed in the field.  
335 There is considerable variation in the GSI in the upper 2.5 m, as well as three distinct increases  
336 in mean grain size and the GSI at 3.4–3.8 m, 4–5 m, and 6–7.5 m (Fig. 2) which occur as  
337 subangular very coarse sand (Table S1). We interpret these peaks as evidence of colluvial input  
338 from the nearby bedrock outcrops, which are c. 0.7 km south of the site. Micromorphological  
339 analysis on six selected samples throughout the profile also identified persistent occurrence of  
340 angular gypsum crystals below 1.6 m depth (Table S1), which should represent *in situ*  
341 precipitation under arid conditions.

342 The exposed outcrop of MAL is 6 m-thick. The uppermost c. 0.4 m is composed of modern soil  
343 with roots developed within colluvial loess-like material. At 0.4–0.9 m depth, we observe fewer  
344 angular clasts within a loess matrix. A discontinuous very coarse sand to gravel layer with silt  
345 matrix was observed at 1.1–1.3 m, below which carbonate-rich loess dominates down to c. 2  
346 m. Below 2 m depth, the section is composed of pale yellowish-beige primary loess, with  
347 occasional carbonate mottling and Fe-Mn concretions observed at 2.5–5 m. The MAL section  
348 yields higher magnetic susceptibility (c.  $70 \times 10^{-8} \text{ m}^3\text{kg}^{-1}$ ) in the upper 1.5 m, most likely  
349 reflecting recent pedogenesis. Mean grain size and GSI vary substantially at 0.5–2.5 m; below  
350 5 m, a sudden decrease in grain size is observed. The grain size variations in the upper 2.5 m  
351 most likely reflect variable colluvial input to the silt-dominated aeolian component. Below 2.5  
352 m, the mean grain size, as well as GSI, does not show significant variation and is likely to reflect  
353 purely aeolian input to the site. The abrupt decrease of GSI in the primary loess below 5 m  
354 most likely indicates a decrease in wind strength (Fig. 2).



355

356 Fig. 2. Stratigraphy of the loess sites under study, with down-profile variation in mean grain  
357 size (GS), grain size index (GSI) and magnetic susceptibility at the respective sites. The grain  
358 size dataset for REM is obtained from Schulte et al. (2018) and the magnetic susceptibility at  
359 REM is from Fitzsimmons et al. (2018).



Table 1. Equivalent dose, dose rate data and luminescence age estimates for fine grained quartz from the Illi basin study sites. The term  $n_e/n_t$  refers to the total number of accepted discs to the total number of discs measured.

Site	Sample No.	Depth (m)	Moisture attenuated dose rate (Gy/ka)			Cosmic (Gy/ka)	Total Dose Rate (Gy/ka)	$n_e/n_t$	De (Gy)	Age (ka)
			Alpha	Beta	Gamma					
Remizovka (REM)	L-EVA-1475	1.1 ± 0.10	0.5 ± 0.1	2.0 ± 0.2	1.2 ± 0.1	0.20 ± 0.02	3.8 ± 0.4	24/24	48.2 ± 0.5	12.8 ± 1.2
	L-EVA-1476	2.1 ± 0.10	0.5 ± 0.1	2.3 ± 0.2	1.3 ± 0.1	0.17 ± 0.02	4.3 ± 0.4	24/24	75.7 ± 1.0	17.8 ± 1.6
	L-EVA-1477	3.1 ± 0.10	0.6 ± 0.1	2.3 ± 0.2	1.4 ± 0.1	0.15 ± 0.02	4.4 ± 0.4	22/24	86.0 ± 1.2	19.7 ± 1.9
	L-EVA-1478	4.1 ± 0.10	0.5 ± 0.1	2.2 ± 0.2	1.3 ± 0.1	0.13 ± 0.01	4.1 ± 0.4	24/24	88.4 ± 1.4	21.7 ± 2.0
	L-EVA-1479	5.1 ± 0.10	0.5 ± 0.1	2.2 ± 0.2	1.2 ± 0.1	0.12 ± 0.01	4.0 ± 0.4	24/24	99.1 ± 1.6	24.9 ± 2.3
	L-EVA-1480	6.1 ± 0.10	0.5 ± 0.1	2.2 ± 0.2	1.2 ± 0.1	0.11 ± 0.01	4.0 ± 0.4	24/24	107.0 ± 2.0	26.5 ± 2.5
	L-EVA-1481	7.1 ± 0.10	0.5 ± 0.1	2.2 ± 0.2	1.3 ± 0.1	0.10 ± 0.01	4.0 ± 0.4	24/24	127.0 ± 2.0	31.5 ± 2.9
Panfilov (PAN)	A0017	1.0 ± 0.05	0.5 ± 0.1	2.2 ± 0.2	1.3 ± 0.1	0.21 ± 0.02	4.2 ± 0.2	19/19	23.1 ± 0.3	5.5 ± 0.3
	A0019	2.0 ± 0.05	0.4 ± 0.1	1.9 ± 0.2	1.1 ± 0.1	0.18 ± 0.02	3.6 ± 0.2	19/19	38.5 ± 0.5	10.6 ± 0.7
	A0021	3.0 ± 0.05	0.5 ± 0.1	2.1 ± 0.2	1.2 ± 0.1	0.16 ± 0.02	3.9 ± 0.2	16/17	47.4 ± 1.8	12.0 ± 1.1
	A0023	4.0 ± 0.05	0.5 ± 0.1	2.0 ± 0.2	1.2 ± 0.1	0.14 ± 0.01	3.9 ± 0.2	20/20	63.4 ± 1.6	16.4 ± 1.3
	A0025	5.0 ± 0.05	0.5 ± 0.1	2.2 ± 0.2	1.3 ± 0.1	0.13 ± 0.01	4.0 ± 0.2	16/17	64.4 ± 2.6	15.9 ± 1.4
Ashubulag (ASH)	A0026	0.5 ± 0.05	0.4 ± 0.1	1.8 ± 0.2	1.1 ± 0.1	0.24 ± 0.02	3.6 ± 0.2	20/20	45.9 ± 0.6	12.9 ± 0.9
	A0028	1.5 ± 0.05	0.5 ± 0.1	2.1 ± 0.2	1.3 ± 0.1	0.20 ± 0.02	4.1 ± 0.2	20/21	52.6 ± 2.0	12.7 ± 1.1
	A0030	2.5 ± 0.05	0.5 ± 0.1	2.2 ± 0.2	1.3 ± 0.1	0.17 ± 0.02	4.2 ± 0.2	19/20	51.1 ± 2.0	12.3 ± 1.1
	A0032	3.5 ± 0.05	0.5 ± 0.1	2.3 ± 0.2	1.3 ± 0.1	0.15 ± 0.02	4.2 ± 0.2	20/20	63.0 ± 1.3	14.9 ± 1.0
	A0034	4.5 ± 0.05	0.5 ± 0.1	2.2 ± 0.2	1.3 ± 0.1	0.14 ± 0.01	4.1 ± 0.2	21/22	63.5 ± 1.1	15.6 ± 1.1
Taukaraturyuk (TAU)	A001	0.5 ± 0.05	0.4 ± 0.0	1.8 ± 0.1	1.1 ± 0.1	0.24 ± 0.02	3.5 ± 0.2	22/22	46.6 ± 1.4	13.3 ± 1.0
	A002	1.0 ± 0.05	0.5 ± 0.1	2.0 ± 0.2	1.2 ± 0.1	0.21 ± 0.02	3.9 ± 0.2	22/22	44.9 ± 0.7	11.4 ± 0.8
	A003*	1.5 ± 0.05	0.5 ± 0.1	2.0 ± 0.1	1.2 ± 0.1	0.19 ± 0.02	3.9 ± 0.2	8/8	305.1 ± 13.8	78.3 ± 7.1
	A0016*	7.5 ± 0.05	0.5 ± 0.1	2.3 ± 0.2	1.3 ± 0.1	0.10 ± 0.01	4.2 ± 0.2	7/11	301.6 ± 22.4	71.5 ± 8.5
Malubai (MAL)	A0037 <sup>†</sup>	1.0 ± 0.05	0.6 ± 0.1	2.0 ± 0.2	1.2 ± 0.1	0.21 ± 0.02	4.0 ± 0.2	3/3	339.7 ± 17.0	84.9 ± 8.5
	A0037*	1.0 ± 0.05	0.8 ± 0.1	2.4 ± 0.2	1.6 ± 0.1	0.20 ± 0.02	5.0 ± 0.2	3/3	339.7 ± 17.0	67.9 ± 6.1
	A0050*	5.1 ± 0.05	0.7 ± 0.1	2.5 ± 0.2	1.6 ± 0.1	0.13 ± 0.01	4.9 ± 0.2	3/3	373.1 ± 18.5	76.1 ± 6.8

<sup>†</sup>A0037 has unusually low Uranium content compared to the samples from the rest of the profile, hence, the age derived here maybe overestimated due to low dose rate. Hence, we use the dose rate of A0038. \* The text shown in Italics are saturated ages from Quartz estimated from dose response curves constructed at high doses



## 364 Chronology of the Zailisky Alatau loess sections, Central Tien Shan piedmont

365 The samples in this study were dated using quartz OSL and polymineral pIRIR dating and a  
366 detailed record of the luminescence characteristics, equivalent dose and dose rate estimations  
367 and age calculations can be found in the SI. The final age estimates from all five loess profiles  
368 in this study are summarised in Table 1 and Fig 3. Fine-grained quartz OSL ages were derived  
369 for 19 samples from four sites (REM, PAN, ASH, and the upper 1m of TAU; Fig 3) The upper 7  
370 m of the profile REM spans 10–40 ka and falls within the uncertainties of previously published  
371 pIRIR ages (Fitzsimmons et al., 2018), while profiles PAN, ASH and the upper 1 m of TAU date  
372 to between 6–17 ka. Polymineral fine-grain pIRIR dating on 8 selected samples from below 1.5  
373 m at TAU and the entire section at MAL yielded minimum age estimates (Table S2), as these  
374 samples exhibited saturation of the pIRIR<sub>290</sub> signal. Hence, we consider the deposition below 1  
375 m at TAU and at MAL occurred >180 ka.

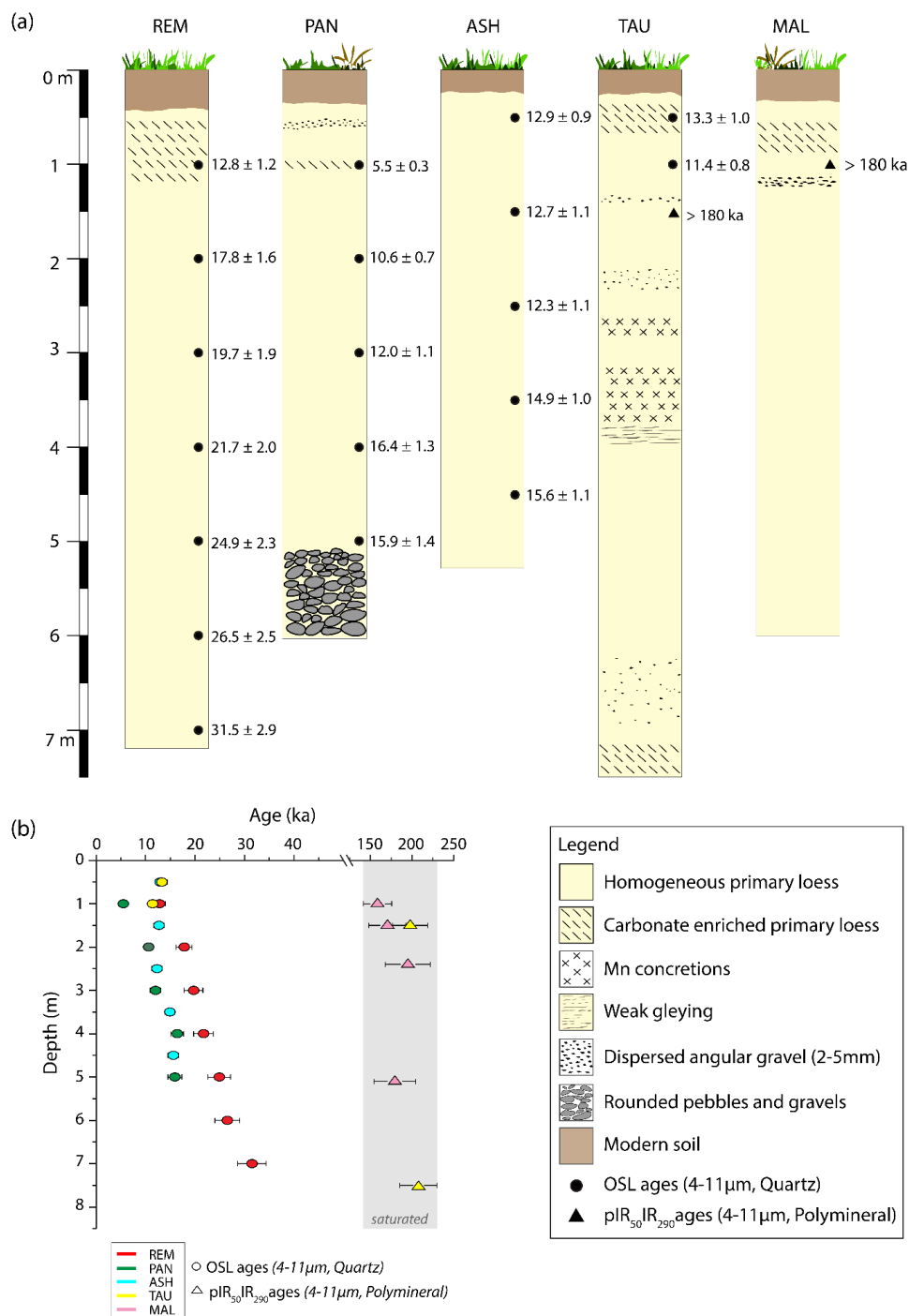
376

## 377 Age modelling and mass accumulation rates

378 Figure 4 shows the location of our sites, as well as of published sites from ACA and CLP, for  
379 which we calculated mass accumulation rates (MARs) from luminescence-based chronologies  
380 (quartz OSL and feldspar pIRIR ages). We limited our calculations of MARs to the last 60 ka since  
381 (i) our investigations suggest an upper limit to reliable dating of quartz in this region (based on  
382 saturation of the quartz OSL signal) of c. 70 ka, and (ii) most published loess sites in ACA and  
383 the CLP span this time period, so allowing for a representative evaluation of loess depositional  
384 dynamics across these regions.

385 The MARs of sites in the Ili Basin, elsewhere in ACA, and across the CLP are illustrated with  
386 respect to concentrations of dust within the Greenland NGRIP ice core (Ruth et al., 2007),  
387 stable oxygen isotope records from NGRIP (Rasmussen et al., 2014) and the global marine stack  
388 (Lisiecki and Raymo, 2005), and June solar insolation at 65°N (Berger and Loutre, 1991) in Fig.  
389 5. We observe substantial differences in absolute accumulation as well as the timing of peaks  
390 in accumulation between sites in the Ili Basin and across ACA more widely (Fig. 5a, b). There  
391 are similar differences across the CLP (Fig. 5c). Furthermore, based on our calculations of MARs  
392 from 11 sites across the CLP, we observe a distinct difference between sites located in the  
393 northwest (NW) and those in the southeast (SE). The geographic difference in loess  
394 accumulation in the CLP has previously been reported for various time periods (Lu and Sun,  
395 2000; Kohfeld and Harrison, 2003; Xu et al., 2018; Liu et al., 2020).

396



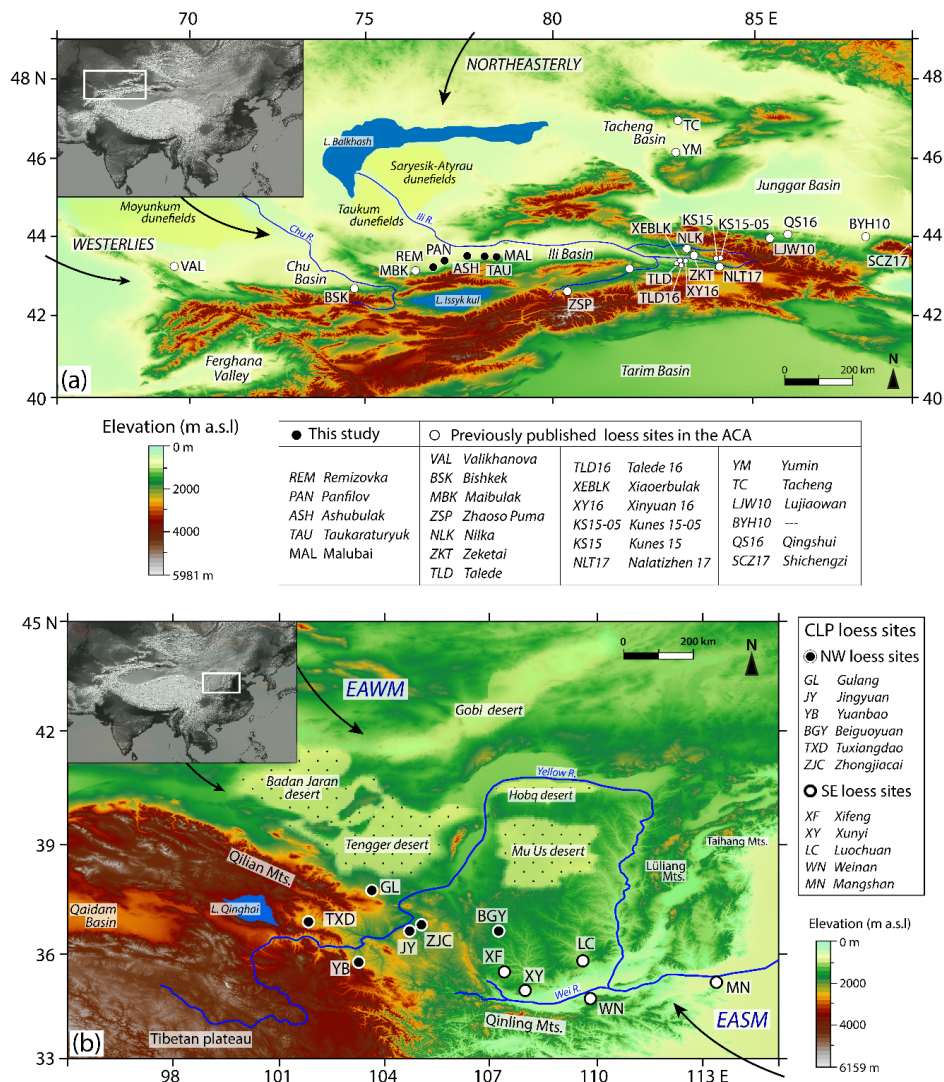
397

398 Fig. 3. (a) Stratigraphy of all the sites with the luminescence ages obtained in this study. (b) Plot  
399 of optical ages (2σ uncertainty) as a function of depth for all sites.



400

401



402

403 Fig 4. Location and regional settings of all reliably dated loess sites in (a) ACA and (b) the CLP,  
404 for which we calculated MARS. References of all the published loess sites are listed in Table S5  
405 of the SI. The elevation map in both cases were created using open source SRTM data provided  
406 by AW3D of the Japan Aerospace Agency.

407

408



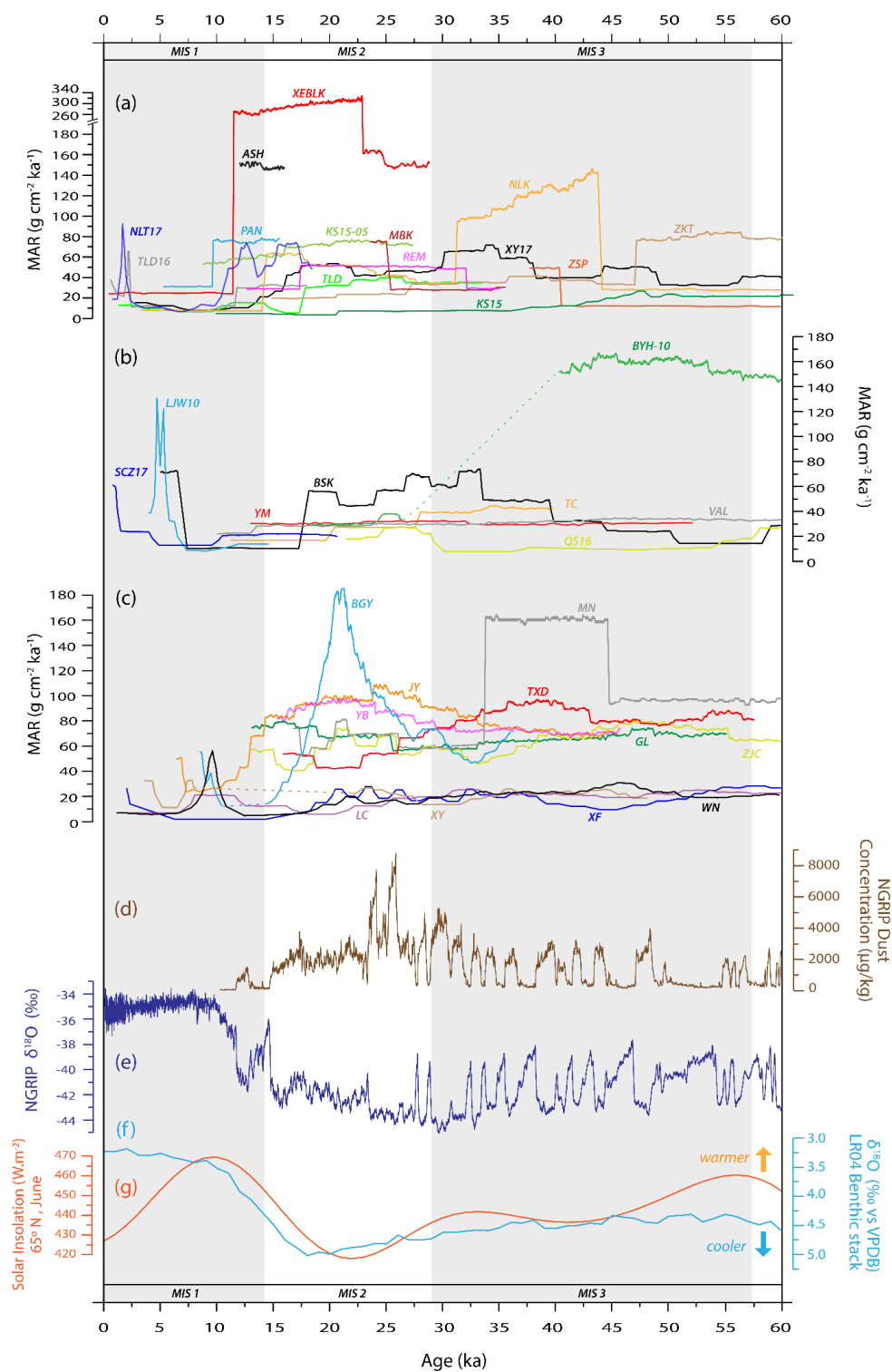




Fig. 5. Comparison of MARs over the past 60 ky for loess sites in (a) the Ili Basin (b) other enclosed basins in ACA and (c) the CLP. Note the uniform y-axis, with the exception of extremely high MARs at XEBLK in the Ili Basin. We compare the loess accumulation rates with (d) NGRIP dust flux (Ruth et al., 2007), (e) NGRIP  $\delta^{18}\text{O}$  (Rasmussen et al., 2014), (f) stacked benthic foraminifera  $\delta^{18}\text{O}$  marine record LR04 (Lisiecki and Raymo, 2005) and (g) June insolation at  $65^\circ\text{N}$  (Berger and Loutre, 1991). The dashed lines in the MARs represents a depositional unconformity/ hiatus at the respective site.

417

## 418 DISCUSSION

### 419 Spatio-temporal variation in loess deposition along the Central Tien Shan (Zailisky 420 Alatau region)

Our new dataset adds chronologic constraints for five loess sites (including new data from REM) from the virtually unexplored Zailisky Alatau piedmont in the western portion of the Ili Basin. Our sites bridge the geographic gap between the relatively intensely studied eastern Ili Basin (E et al., 2012; Kang et al., 2015; Song et al., 2012, 2015; Li et al., 2016b, 2018a; Wang et al., 2019a,b; Li et al., 2020), and several dated sites further west at Maibulak (MBK) – also along the Zailisky Alatau (Fitzsimmons et al., 2017), Bishkek (BSK) in the Chu River valley (Youn et al., 2014) and Valikhanova (VAL) on the eastern slopes of the Karatau Range (Fitzsimmons et al., 2017) (Fig 5a).

429

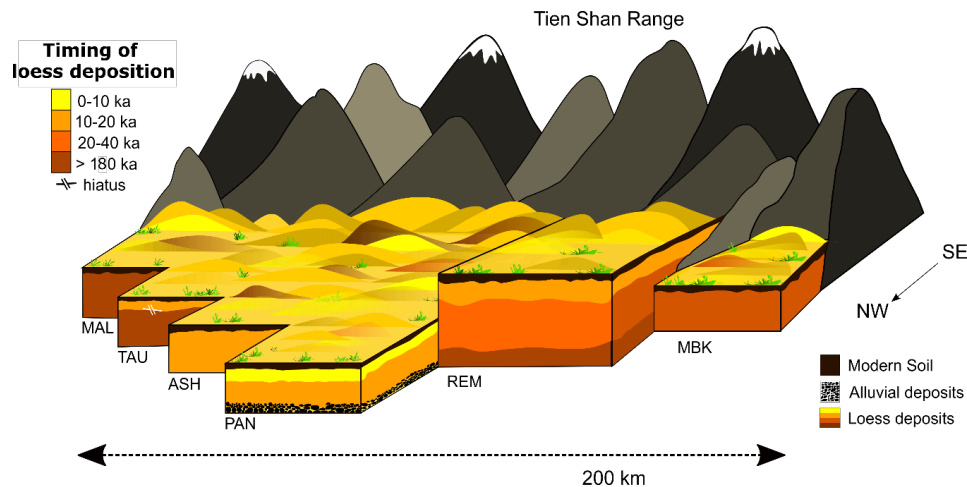
We identified phases of loess accumulation and illustrated these with respect to altitude, deposit thickness and distance from the range front in a schematic diagram in Fig. 6. Geographically, the four sites of MBK, REM, PAN and ASH lie west of the Ili Gate and in the more open part of the basin. TAU and MAL lie at approximately the narrowest part of the basin (the “Gate”) and are comparatively sheltered from northerly winds. The sites of PAN, ASH, TAU and MAL lie at similar elevations (c.700-800 m a.s.l.); both MBK and REM are situated at higher altitudes (1070 m a.s.l.). The distances of the sites from the range front are also variable. MBK in the west overlies an alluvial fan c. 350 m from the range front and c. 2 km northward of a steeper break in slope. REM is situated atop a spur of the foothills which rises c. 200 vertical metres above the plain, and c. 5 km from the major break in slope representing the transition to bedrock ranges. PAN and ASH lie the greatest distance from the range front, c. 7.5-8 km to its north. TAU is located c. 1 km northward of the first ridge of the Zailisky Alatau, and MAL lies c. 150 m north of a bedrock spur and c. 2.3 km north of the main range. With the exception of REM, where the range front is oriented approximately SSW-NNE, all sites are situated northward of an east-west trending break in slope. We hypothesise that (1) location within the basin, (2) distance from the range front and (3) its strike are all likely to have played a role in the potential of individual sites to trap aeolian sediment through time.

447

448



449



450

451 Fig. 6. Schematic 3D representation of the timing of loess accumulation phases along the  
452 Zailisky Alatau range in the Central Tien Shan, southeast Kazakhstan.

453

454

455 The westernmost sites, MBK and REM, range in age between 12–45 ka (this study; Fitzsimmons  
456 et al., 2017, 2018). Although the loess at REM extends downward toward older ages (Machalett  
457 et al., 2006; Sprafke et al., 2018), the lack of high-resolution dating >45 ka prevents our  
458 consideration of accumulation during earlier periods. By contrast, the two central sites, PAN  
459 and ASH, are substantially younger in age and span much shorter periods of time; 17–5 ka and  
460 15–12 ka respectively. The site of TAU, situated c. 20 km east of ASH, preserves c. 1 m of loess  
461 accumulation during a similar time period to ASH (c. 11–13 ka) and overlies an unconformity  
462 with substantial hiatus, below which the loess exceeds 180 ka. The easternmost Zailisky Alatau  
463 site of MAL pre-dates 180 ka and yielded no Late Pleistocene deposits. We hypothesise that  
464 the location of TAU and MAL within the more sheltered Ili Gate area led to reduced loess  
465 accumulation over the late Pleistocene compared with the more exposed western sites.  
466 Increased wind strength related to a “funnelling” effect by the enclosing mountain ranges may  
467 also have led to the erosional unconformities observed at TAU and MAL.

468

469 While loess grain size is often used as a proxy for wind intensity through time (An et al., 1991a;  
470 Porter and An, 1995; Sun and An, 2005; Vandenberghe et al., 2013), our observations from the  
471 Ili Basin loess deposits strongly suggest that additional controls, such as geomorphic setting,  
472 sediment availability and supply to individual sites, also influence aeolian flux and grain size.  
473 We compared changes in GSI from three study sites (REM, PAN and ASH) with those from the  
474 published site of NLK in the eastern part of the basin (Li et al., 2018c), focussing on the time  
475 period c. 12–16 ka (Fig. 7). GSI values during this interval range from 0.30–0.40 at REM, 0.40–  
476 0.65 at PAN, 0.25–0.45 at ASH, and 0.30–0.60 at NLK. We observe that not only the magnitude



of variability in GSI but also the mean value differs between sites. Sediments at PAN are coarser than at ASH, despite the relative proximity of these two sites. GSI values are less variable at REM in the west, than at NLK in the east (Fig. 7). These differences within the same time interval along the piedmont suggest spatial variability in sediment supply, transport to and deposition at an individual site. For example, the proximity of both NLK and PAN to active fluvial channels may account for relatively greater amounts of proximal transport of coarser grains (Li et al., 2018c) than can be transported to the other sites. The higher elevation of REM relative to the other sites may account for the overall finer GSI values and smaller range of GSI at the site reflecting a greater reliance on distal transport and sorting.

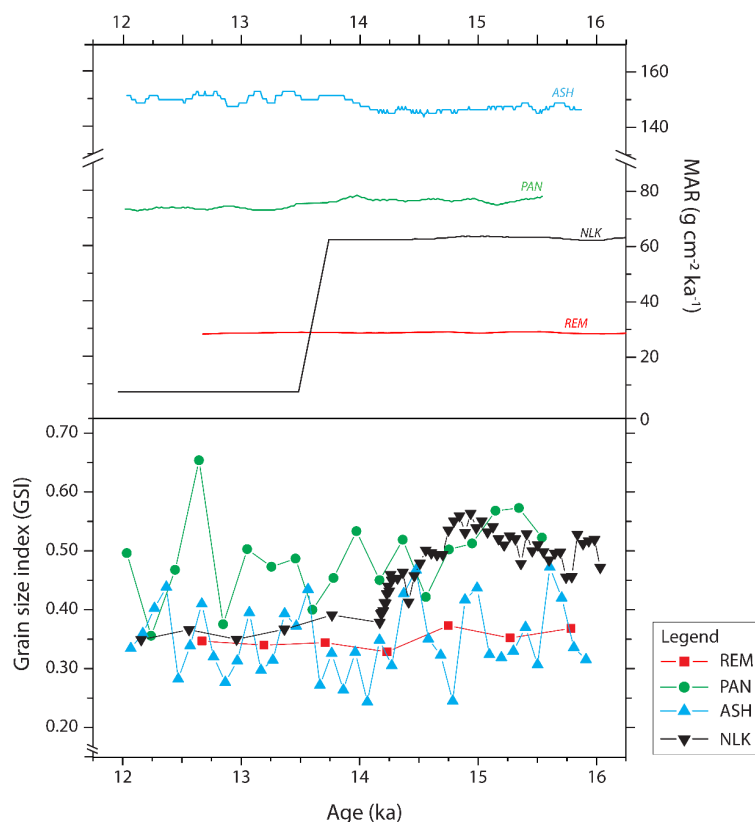


Fig. 7. Comparison of MAR and GSI for late MIS2 (12–16 ka) from four loess sites (REM, PAN, ASH and NLK) from an east-west transect along the Zailiysky Alatau, SE Kazakhstan. The GSI for NLK were calculated from published data (Li et al., 2018c).

The geomorphic context of individual sites is likely to influence not only grain size characteristics and variability through time, but also aeolian flux, expressed here as MARs (Fig.



7). For the 12–16 ka time period, aeolian flux at ASH far exceeds that at any other site, with PAN experiencing the next highest rate of accumulation. We suggest that its relatively low elevation, distance from alluvial fans and range front, and a strengthened westerly trajectory of dust-laden winds at the Ili Gate resulted in higher accumulation here than at any other site along the piedmont for which we have data. On the other hand, whilst MARs at PAN are lower than at nearby ASH, its GSI range is higher and may reflect greater inmixing of proximal fluvial material with distal accumulation. This observation raises questions regarding hitherto popular correlation of proxies such as grain size and aeolian flux with wind strength in loess deposits generally. The older deposits at MAL and TAU yield GSIs in the 0.4–0.9 range, which is greater than that observed at the other sites. This may relate to the proximity of TAU and MAL to a seismically active range front (Chilik fault), which can introduce coarser clasts to the loess via slope transport. These observations highlight the need to first interrogate the geomorphic setting of individual sites for their potential to reflect local or larger scale processes according to proposed research questions.

We observe along the Zailisky Alatau transect, a ‘patchwork’ loess piedmont of spatially variable timing of peaks in deposition, flux and grain size. This most likely reflects the result of complex interactions between local and continental wind regimes and associated dust transport, topographic (including palaeotopographic) context, and local sediment supply.

### **Loess sedimentation dynamics across the Ili Basin: Overcoming individual site bias to reconstruct the interplay between the Westerlies and Siberian High Pressure system**

The ACA piedmonts, especially the Ili Basin, lie at a pivotal topographic point which exposes the region both to the mid-latitude Westerly winds and the Siberian High Pressure, the latter manifesting here in the form of northerly winds associated with the seasonal migration of the high-altitude polar jet (Fitzsimmons et al., 2020). The Westerlies rarely penetrate eastward of the Tien Shan range; loess deposited in this part of ACA therefore represents a strategic record of aeolian transport and deposition associated with both climate subsystems. Published correlations from the eastern Ili Basin loess linking grain size with penetration of westerly air flow suggest that the influence of the Westerlies was neither consistent nor strong over the Late Pleistocene (Li et al., 2018c). The loess deposits of the Ili Gate/Zailisky Alatau region investigated in this study, coupled with data from the eastern Ili Basin, can provide more meaningful information relating to the interplay between the Westerlies and Siberian High climate systems through time.

Here we examine the degree to which loess profiles across the entire Ili Basin record past environmental conditions in the form of accumulation rates. In Fig. 5a, we show MARs from our new datasets from REM, PAN and ASH, in addition to those from 11 published sites (E et al., 2012; Kang et al., 2015; Song et al., 2012; 2015; Li et al., 2016b 2018a, 2020; Fitzsimmons



et al., 2017, 2018; Wang et al., 2019a,b), presenting a 60 ka record from the eastern headwaters of the Basin to the 'Ili Gate'.

We observe substantial differences in absolute MAR's between sites, not only over the 60 karange but also over shorter timescales such as the deglacial and MIS 3 interstadials. We hypothesise that absolute MAR's are likely to reflect differences in topographic settings between individual sites. Absolute sedimentation rates at NLK, for example, are approximately five times those observed at the sites KS15 and XY17 during late MIS 3 (40 – 27 ka). NLK is located on the banks of the Kax River (Kashi; Song et al., 2015), whereas KS15 is located in the easternmost Ili Basin and on the upper terraces of the Kunes River (Li et al., 2018a). While both these rivers, tributaries of the Ili, derive from glacial sources, the closer proximity of NLK to the river banks implies a higher sediment availability during MIS 3, when glaciers in the Tien Shan expanded in response to increased moisture transport to ACA (Koppes et al., 2008). The topographic setting of KS15 is also likely to have resulted in relatively low aeolian flux during other time periods. The site KS15-05 (Wang et al., 2019a), located c. 3 km east of KS15 (Fig. 5 and Fig 6a), yielded MARs three times higher than at KS15 during late MIS 2 and early MIS 1 and is likely to relate to the closer proximity of the former to the active river channel.

There is also considerable variability in the timing of peaks in loess accumulation across the basin. For example, despite the proximity of the two eastern Ili Basin sites NLK and ZKT (Fig. 5a), the former yields peak MARs during late MIS3 (c. 45-30 ka) and the latter peaks during early MIS3 (c. 60-47 ka). These site-specific variations in loess sedimentation rates raise questions regarding how representative the MARs of individual sites may be for understanding regional climatic variations. We propose instead that aggregated trends in loess MARs from multiple sites across a basin are more likely to reflect changes in climate dynamics, so providing the best means to overcome the bias of individual sites based on their local setting.

We observe generally increased sedimentation across the entire Ili Basin during interstadial MIS 3 (29–57 ka; Lisiecki and Raymo, 2005); this extends on findings from previous studies which noted primary loess accumulation at this time in the Zailisky Alatau area (Fitzsimmons et al., 2018). Fitzsimmons et al. (2018) hypothesised that increased loess flux during late MIS 3 (c. 40–27 ka) was due to general increased sediment availability and wind strength at this time. Increased sediment supply was likely to be linked to glacial advances in northern and eastern Tien Shan (Kong et al., 2009; Li et al., 2011, 2014; Chen et al., 2015) driven by increased moisture transport by the Westerlies, and also recorded in weak pedogenesis within the loess (Song et al., 2012, 2015; Fitzsimmons et al., 2018). Furthermore, it has been proposed that the Siberian High, which intensified during late MIS 3 (Ding et al., 1995; Hao et al., 2012), would have compressed the Westerlies against the Tien Shan ranges and increased wind strength into the Ili valley (Fitzsimmons et al., 2018). The combination of increased sediment availability and wind strength in the Ili Basin would therefore have contributed to the increased loess accumulation observed in aggregate during this period (Fig 7a). Local katabatic winds might also have played an important role during this phase, resulting in localised effects on the timing and peaks of loess sedimentation.



We also observe generally increased accumulation rates in aggregate during MIS 2 (29–14 ka, Lisiecki and Raymo, 2005) (Fig. 5a). These conditions coincide with globally cold climates prevailing during the Last Glacial Maximum (26–19 ka LGM; Clark et al., 2009). In the Ili Basin the conditions were not only cooler, but also more arid: stable carbon isotopic ( $\delta_{13}C_{org}$ ) reconstructions for palaeovegetation in the valley indicate an increase in more arid-adapted  $C_4$  vegetation (Ran and Feng, 2014). Cold, dry, windy climate appears to have resulted in coarser grain sizes within a number of loess sequences across the Ili Basin (Song et al., 2015; Li et al., 2016b, 2018c). Climate simulations models indicate windier LGM conditions, due either to stronger mid-latitude Westerlies (Sun et al., 2012) or intensified Siberian High pressure (Cheng et al., 2021). Glacial expansion during MIS 2 in the Central and Eastern Tien Shan (Kong et al., 2009; Li et al., 2011; 2014; Lifton et al., 2014; Blomdin et al., 2016), also resulted in increased production of silt, therefore according availability within the Ili catchments for dust entrainment and transport.

Our analyses also suggest relatively widespread increase in MARs across most Ili Basin sites during the warming conditions of the global deglacial period (19–11 ka, Clark et al., 2012) (Fig. 5a). Those sites which do not show any increase (KS15 and ZSP) are likely to be more influenced by their topographic setting; both are located in the easternmost or upper reaches of the basin with minimal exposure to Westerly air flow (and in general records very low accumulation rates). Elsewhere, short-lived phases of increased flux of coarser grain size fractions have been correlated to abrupt climatic events such as the Younger Dryas (c. 12–11 ka) at several sites during the deglacial period (e.g. NLK: Li et al., 2018c; XEBLK: Li et al., 2016b), and have been hypothesised to associate with increased Westerly penetration eastward into the Ili Basin. Climate simulations (Wyrwoll et al., 2016) suggest that the strength of the Siberian High was reduced at this time. Such conditions would have increased the influence of the Westerlies on the Ili Basin, including increasing rainfall; increased deglacial moisture availability is supported by more dominant  $C_3$  vegetation signatures in the basin (Ran and Feng, 2014). We suggest that sediment availability was greater than during the LGM due to increased runoff promoted both by glacial melt under warmer conditions and increased precipitation transported by the Westerlies.

602

## **Variability in loess accumulation rates across mid-latitude Asia: Implications for interpreting loess archives from Central Asia to the Chinese Loess Plateau**

Continental mid-latitude Asia, with its extensive deserts and widespread loess deposits, is believed to be one of the major contributors to the global dust cycle (Narsima, 2007; Kok et al., 2021). It is therefore imperative that we better understand the processes driving dust flux and their contribution to Northern Hemisphere climate dynamics. One major step towards our understanding of these processes involves quantifying Quaternary dust accumulation. Loess MARs provide the closest approximation of the ‘dust parameter’ over Pleistocene timescales. Given the issues raised by our analysis of the Ili Basin piedmont deposits, we compared loess





MARs elsewhere in continental mid-latitude Asia over the same time period (0–60 ka), with a focus on the Chinese Loess Plateau (CLP) and published sites across ACA more widely. In doing so we further assess spatial and temporal inhomogeneity in loess MARs and the degree to which regional characteristics such as topography and climate influence MARs.

The CLP of central northern China was the first loess region to be recognised as a significant terrestrial palaeoclimate archive (Liu, 1962), and is now one of the most intensively studied loess areas in the world (An et al., 1991a,b; Porter and An, 1995; Ding et al., 2002; Kohfeld and Harrison, 2003; Sun and An, 2005; Stevens et al., 2008, 2013, 2018). Unlike the Central Asian piedmonts, the CLP forms an extensive, continuous plateau exceeding 200 m thickness in parts and centred on the southern half of the Ordos Loop of the Yellow River (Yang and Ding, 2010). The loess is believed to derive from denudation associated with uplift of the Tibetan highlands (Sun and Liu, 2000; Sun, 2002; Smalley et al 2014); its connection with the ice sheets of the Tibetan “third pole” underpins the assumption linking primary loess with glacial phases. The dominant sources of loess to the CLP are sediments derived from the Tibetan plateau, transported by the Yellow River prior to entrainment as dust (Stevens et al., 2013; Nie et al., 2015; 2018; Bird et al 2015; 2020); a significant proportion is recycled along the length of the river system as it flows along the plateau (Licht et al., 2016). The climate of the CLP is strongly influenced by the East Asian winter and summer monsoons (EAWM and EASM respectively). Northwesterly winds associated with the Siberian High Pressure system produce cold, dry, dust-bearing EAWM winter conditions (Liu and Ding, 1998; Maher, 2016), which alternate with rain-bearing southeasterly EASM summer monsoonal air flow (An et al., 1991b; Yang et al., 2015). Grain size analyses suggest that loess particles coarsen with strengthening EAWM during glacial conditions (Sun et al., 2012; Stevens et al., 2018). Several studies report a southeastward decrease in loess flux which correlates with decreasing grain size, and has been linked to the strength of the EAWM (Lu and Sun, 2000; Vriend et al., 2011; Liu et al., 2020). However, several high-resolution luminescence dating studies challenge the prevailing assumption that CLP loess accumulation is uniformly driven by the strength of the EAWM (Stevens et al., 2006, 2007; Xu et al., 2018).

Fig. 5c shows MARs from 11 selected sites (Lai and Wintle, 2006; Lu et al., 2007 Stevens et al., 2008, 2016; Buylaert et al., 2008; Sun et al., 2012; Kang et al., 2013; Qiu and Zhou, 2015; Fig. 5b) across the CLP, following a northwest-southeast (NW-SE) transect over the period c. 0–60 ka. We observe a distinct difference in net loess accumulation, as well as in the timing in peak MARs, between the northwest and southeast sites. MARs in the northwestern sites are approximately three times higher than those in the southeast.

As we observed for the sites in the Ili Basin, the geomorphic context in the CLP appears to influence both absolute accumulation and timing of peaks in accumulation at individual sites. For example, among northwestern sites, JY shows higher accumulation rates than ZJC and GL, and likely relates to the proximity to the Yellow River; JY is located on the upper terraces of the



river, whereas ZJC and GL are both situated further from fluvial source, south and north of the river respectively. In contrast to the generally low accumulation rates of the southeastern sector, the site of MN, located on the banks of the Yellow River, has net accumulation comparable to the northwestern sites (Qui and Zhou, 2015; see Fig. 5c). In general, sites in close proximity to the Yellow River, as well as those close to the desert deflation zones, record higher MARs than those more distal to these likely sources. It appears that despite the role of the EAWM as a dust transport vector (Vriend et al, 2011; Liu et al., 2020), net accumulation of loess across the CLP is also locally influenced by proximity to source sediment, whether fluvial or aeolian. Nevertheless, desert marginal sites, such as Jingbian (Stevens et al., 2018), also record erosional unconformities; this effect has been proposed to result from increased erosional capacity of the EAWM in those regions. Not all records of MARs can be easily explained by climate mechanisms or by geomorphic context, however; the extremely high MAR at BGY during LGM (Fig. 6c) may relate to local preservation potential associated with expansion and contraction of the EASM (Buylaert et al., 2008).

The timing of MAR peaks in aggregate across the CLP gives a more nuanced insight into the climate dynamics acting in the region than previously obtained. We observe a divergence in the timing of peaks in loess accumulation between the northwest and southeast. In the northwest, loess accumulation increases during c. 18–11 ka and decreases at c. 11–6 ka (Fig. 5c), whereas the opposite is observed in the southeast sites. This alternating pattern has previously been attributed to a persistent weakening of the EAWM and gradual strengthening of the EASM during the early Holocene, with the opposite proposed for the deglacial (Xu et al., 2018; Kang et al., 2020). We suggest that the increase in MARs of the CLP southeastern sites during early Holocene may relate to their proximity to the Wei River, which drains the Qinling Mountains and is more strongly influenced by the EASM; aeolian flux in this region would therefore respond more closely to sediment availability relating to increased runoff during strengthened monsoon conditions. Overall, the CLP experienced an increase in MARs during the LGM and is consistent with widespread glaciation on the Tibetan Plateau (Owen et al., 2003a,b, 2006; Owen and Dortsch, 2014), although relative changes in the southeast sites was less pronounced, likely due to distance from the Yellow River and northern deserts. Loess MARs decreased altogether during MIS 3 (c. 57–29 ka, Lisiecki and Raymo, 2005), most likely due to relatively weakened EAWM wind strength, although sediment supply was sustained by suspended load fluvial outwash linked to glaciations on the Tibetan plateau (Owen et al., 2003a; Owen and Dortch, 2014; Rother et al., 2017) in response to increased monsoonal precipitation. The sustained supply of sediment to the CLP can be observed in the generally higher MARs at the northwestern sites proximal to the river.

In addition to our analyses of MARs across the Ili Basin and CLP, we also calculated MARs from 8 other published loess sites across ACA (Fig. 4 and Fig. 5b). These sites not only represent similar piedmont settings to those found in the Ili Basin but are also influenced by similar climatic contexts. The westernmost sites of BSK (Youn et al., 2014) and VAL (Fitzsimmons et



al., 2017) lie in the foothills of the Kyrgyz Tien Shan and Karatau Range respectively (Fig. 4a). The sites of LJW10 (Li et al., 2015), SCZ17 (Duan et al., 2020) and BYH10 (Li et al., 2016a) are located along the northern piedmonts of the eastern Tian Shan, south of the Junggar Basin (and the Gurbantunggut desert), and TC and YM are situated in the westward opening Tacheng Basin, bound by the northern edge of the Dzungarian Alatau and the Tarbagatai Range to the north (Fig. 4a; Li et al., 2019b)

As observed elsewhere, both absolute MAR values and the timing of peak accumulation are highly variable across the greater ACA. In the west, BSK experienced increased accumulation during late MIS3, continuing into the LGM, while VAL yields substantially lower MARs which remained consistent from late MIS 3 into the LGM. The higher accumulation rates at BSK are most likely due to its proximity to the glacially derived Chu river. Glacial expansion in the Kyrgyz Tien Shan during MIS 3 (Koppes et al., 2008) likely generated the fine-grained sediment for loess deposition at BSK, whereas the Karatau Range, from which the VAL sediments were sourced, was never glaciated and is much more arid, resulting in substantially less sediment supply. Both Tacheng Basin sites yield low, almost constant MARs (c. 30-40 g cm<sup>-2</sup>ka<sup>-1</sup>) throughout the past c. 60 ky (Li et al., 2019b). It is likely that these records relate to the lack of glaciation in the surrounding mountains, resulting in a dependence on the desert to the west as a source of dust (Li et al., 2019b). By contrast, the sites located in the Northern Tien Shan foothills yield variable depositional characteristics (Fig. 4a and Fig. 5b). The site of QS-16 yielded an LGM peak in accumulation; by comparison, the site of BYH-10, located further east, experienced peak MARs from early to mid-MIS 3 an order of magnitude greater than at QS-16, followed by a hiatus and subsequent LGM MAR values comparable with QS-16. LGM deposition in the northern Tien Shan area has been linked to regionally arid conditions and strengthened Westerlies which increased aeolian flux (Li et al., 2016a, 2020). The substantial difference in absolute MAR values at BYH-10 and QS-16 is most likely linked to their individual topographic and geomorphic setting; the former is located on the exposed northern piedmont of the Bogda Shan (eastern Tien Shan) which drains a number of glacially fed rivers, whereas QS-16 is sheltered from the prevailing westerly winds by the Borohoro mountains and is at a greater distance from the northern dust source regions.

It is clear from our MAR review of the Ili Basin, wider ACA, and CLP that absolute accumulation rates and timing at a given site may be influenced by both synoptic-scale climate and local geomorphic settings in the form of proximity to dust sources, topography and sediment availability. At the same time, the timing of peaks in loess accumulation as an aggregate of multiple sites represents a reliable response to climate.

## CONCLUSION

This study provides high resolution chronological frameworks for five new loess sites in the vastly understudied piedmonts of the Zailisky-Alatau (Central Tien Shan). Our new dataset provides the spatial coverage necessary to interrogate the timing and rate of loess deposition



735 along the Ili Basin piedmonts as a whole, whereas previously only the eastern part of the basin  
736 and isolated western sites could be analysed. We observe substantial variability in the timing  
737 and rate of loess deposition across our new sites, which raises questions regarding to what  
738 degree the timing and rate of accumulation at individual sites can be taken as an indicator of  
739 past climate in this region. Our observations across the Ili Basin as a whole indicate a patchwork  
740 of loess deposition. Absolute sedimentation rates at a given site respond both to local  
741 topographic context and sediment availability and to climate. The timing of peaks in  
742 accumulation, irrespective of absolute MAR values and particularly when viewed in aggregate  
743 across a number of sites, represent a response to variability in wind dynamics driven by the  
744 Northern Hemispheric climate subsystems. This interpretation was supported by our analyses  
745 of MAR's from loess sites across wider ACA and the CLP over the past 60 ka. We find that  
746 aggregate MARs from multiple sites provide a more robust tool for understanding past climate  
747 dynamics across a region and overcomes individual site bias.

748

## 749 ACKNOWLEDGEMENTS

750 AKD would like to gratefully acknowledge the following persons and institutions for their  
751 support: Steffi Hesse and Victoria Krippner at the Max Planck Institute for Evolutionary  
752 Anthropology (MPI-EVA), Leipzig, Germany, for access to the HF laboratory, and Giovanni  
753 Muttoni for the use of magnetic susceptibility measurement facilities at the Alpine  
754 Palaeomagnetism Laboratory (Peveragno, Italy). Thanks also to A. Umarkhojiyev, A. Kossenko,  
755 and A. Sirch for assistance in the field. This study was also supported by internal program No.  
756 RVO67985831 of the Institute of Geology CAS, Prague. This study was funded by an  
757 independent Max Planck Research Group awarded by the Max Planck Society to KEF.

758

## 759 REFERENCES

- 760 Albani, S., & Mahowald, N. M. (2019). Paleodust Insights into Dust Impacts on Climate. *Journal*  
761 *of Climate*, 32(22), 7897–7913. doi: 10.1175/JCLI-D-18-0742.1  
762
- 763 An, ZhiSheng, Kukla, G., Porter, S. C., & Xiao, J. (1991)a. Late quaternary dust flow on the  
764 Chinese Loess Plateau. *Catena*, 18(2), 125–132. doi: 10.1016/0341-8162(91)90012-M  
765
- 766 An, Zhisheng, Kukla, G. J., Porter, S. C., & Xiao, J. (1991)b. Magnetic susceptibility evidence of  
767 monsoon variation on the Loess Plateau of central China during the last 130,000 years.  
768 *Quaternary Research*, 36(1), 29–36. doi: 10.1016/0033-5894(91)90015-W  
769



- 770 Andreae, M. O., & Rosenfeld, D. (2008). Aerosol–cloud–precipitation interactions. Part 1. The  
771 nature and sources of cloud-active aerosols. *Earth-Science Reviews*, 89(1), 13–41. doi:  
772 <https://doi.org/10.1016/j.earscirev.2008.03.001>  
773
- 774 Antoine, P., Rousseau, D.-D., Moine, O., Kunesch, S., Hatté, C., Lang, A., Tissoux, H., & Zöller, L.  
775 (2009). Rapid and cyclic aeolian deposition during the Last Glacial in European loess: A high-  
776 resolution record from Nussloch, Germany. *Quaternary Science Reviews*, 28(25), 2955–2973.  
777 <https://doi.org/10.1016/j.quascirev.2009.08.001>  
778
- 779 Arimoto, R. (2001). Eolian dust and climate: Relationships to sources, tropospheric chemistry,  
780 transport and deposition. *Earth-Science Reviews*, 54(1), 29–42. doi:  
781 [https://doi.org/10.1016/S0012-8252\(01\)00040-X](https://doi.org/10.1016/S0012-8252(01)00040-X)  
782
- 783 Avram, A., Constantin, D., Veres, D., Kelemen, S., Obreht, I., Hambach, U., Marković, S. B., &  
784 Timar-Gabor, A. (2020). Testing polymineral post-IR IRSL and quartz SAR-OSL protocols on  
785 Middle to Late Pleistocene loess at Batajnica, Serbia. *Boreas*, 49(3), 615–633.  
786 <https://doi.org/10.1111/bor.12442>  
787
- 788 Banerjee, D., Murray, A. S., Bøtter-Jensen, L., & Lang, A. (2001). Equivalent dose estimation  
789 using a single aliquot of polymineral fine grains. *Radiation Measurements*, 33(1), 73–94. doi:  
790 [10.1016/S1350-4487\(00\)00101-3](https://doi.org/10.1016/S1350-4487(00)00101-3)  
791
- 792 Berger, A., & Loutre, M. F. (1991). Insolation values for the climate of the last 10 million years.  
793 *Quaternary Science Reviews*, 10(4), 297–317. doi: [10.1016/0277-3791\(91\)90033-Q](https://doi.org/10.1016/0277-3791(91)90033-Q)  
794
- 795 Bird, A., Stevens, T., Rittner, M., Vermeesch, P., Carter, A., Andò, S., Garzanti, E., Lu, H., Nie, J.,  
796 Zeng, L., Zhang, H., & Xu, Z. (2015). Quaternary dust source variation across the Chinese Loess  
797 Plateau. *Palaeogeography, Palaeoclimatology, Palaeoecology*, 435, 254–264.  
798 <https://doi.org/10.1016/j.palaeo.2015.06.024>  
799
- 800 Bird, A., Millar, I., Rodenburg, T., Stevens, T., Rittner, M., Vermeesch, P., & Lu, H. (2020). A  
801 constant Chinese Loess Plateau dust source since the late Miocene. *Quaternary Science*  
802 *Reviews*, 227, 106042. doi: [10.1016/j.quascirev.2019.106042](https://doi.org/10.1016/j.quascirev.2019.106042)  
803
- 804 Blaauw, M., & Christen, J. A. (2011). Flexible paleoclimate age-depth models using an  
805 autoregressive gamma process. *Bayesian Analysis*, 6(3), 457–474. doi: [10.1214/11-BA618](https://doi.org/10.1214/11-BA618)  
806
- 807 Blomdin, R., Stroeve, A. P., Harbor, J. M., Lifton, N. A., Heyman, J., Gribenski, N., Petrakov, D.  
808 A., Caffee, M. W., Ivanov, M. N., Hätteland, C., Rogozhina, I., & Usabaliev, R. (2016).  
809 Evaluating the timing of former glacier expansions in the Tian Shan: A key step towards robust



- 810 spatial correlations. *Quaternary Science Reviews*, 153, 78–96.  
811 <https://doi.org/10.1016/j.quascirev.2016.07.029>  
812
- 813 Blott, S. J., & Pye, K. (2001). GRADISTAT: a grain size distribution and statistics package for the  
814 analysis of unconsolidated sediments. *Earth Surface Processes and Landforms*, 26(11), 1237–  
815 1248. doi: <https://doi.org/10.1002/esp.261>  
816
- 817 Buylaert, J. P., Murray, A. S., Vandenberghe, D., Vriend, M., Corte, F. D., & haute, P. V. den.  
818 (2008). Optical dating of Chinese loess using sand-sized quartz: Establishing a time frame for  
819 Late Pleistocene climate changes in the western part of the Chinese Loess Plateau. *Quaternary*  
820 *Geochronology*, 3(1), 99–113. doi: <https://doi.org/10.1016/j.quageo.2007.05.003>  
821
- 822 Buylaert, J.-P., Jain, M., Murray, A. S., Thomsen, K. J., Thiel, C., & Sohbati, R. (2012). A robust  
823 feldspar luminescence dating method for Middle and Late Pleistocene sediments. *Boreas*,  
824 41(3), 435–451. doi: <https://doi.org/10.1111/j.1502-3885.2012.00248.x>  
825
- 826 Buylaert, J.-P., Yeo, E.-Y., Thiel, C., Yi, S., Stevens, T., Thompson, W., Frechen, M., Murray, A., &  
827 Lu, H. (2015). A detailed post-IR IRSL chronology for the last interglacial soil at the Jingbian  
828 loess site (northern China). *LED14 Proceedings*, 30, 194–199.  
829 <https://doi.org/10.1016/j.quageo.2015.02.022>  
830
- 831 Chen, Y., Li, Y., Wang, Y., Zhang, M., Cui, Z., Yi, C., & Liu, G. (2015). Late Quaternary glacial  
832 history of the Karlik Range, easternmost Tian Shan, derived from  $^{10}\text{Be}$  surface exposure and  
833 optically stimulated luminescence datings. *Quaternary Science Reviews*, 115, 17–27. doi:  
834 [10.1016/j.quascirev.2015.02.010](https://doi.org/10.1016/j.quascirev.2015.02.010)  
835
- 836 Cheng, L., Song, Y., Wu, Y., Liu, Y., Liu, H., Chang, H., Zong, X., & Kang, S. (2021). Drivers for  
837 Asynchronous Patterns of Dust Accumulation in Central and Eastern Asia and in Greenland  
838 During the Last Glacial Maximum. *Geophysical Research Letters*, 48(5).  
839 <https://doi.org/10.1029/2020GL091194>  
840
- 841 E, ChongYi., Lai, Z., Sun, Y., Hou, G., Yu, L., & Wu, C. (2012). A luminescence dating study of  
842 loess deposits from the Yili River basin in western China. *Quaternary Geochronology*, 10, 50–  
843 55. doi: <https://doi.org/10.1016/j.quageo.2012.04.022>  
844
- 845 Clark, P. U., Dyke, A. S., Shakun, J. D., Carlson, A. E., Clark, J., Wohlfarth, B., Mitrovica, J. X.,  
846 Hostetler, S. W., & McCabe, A. M. (2009). The Last Glacial Maximum. *Science*, 325(5941), 710.  
847 <https://doi.org/10.1126/science.1172873>  
848
- 849 Clark, P. U., Shakun, J. D., Baker, P. A., Bartlein, P. J., Brewer, S., Brook, E., Carlson, A. E., Cheng,  
850 H., Kaufman, D. S., Liu, Z., Marchitto, T. M., Mix, A. C., Morrill, C., Otto-Bliesner, B. L., Pahnke,



- 851 K., Russell, J. M., Whitlock, C., Adkins, J. F., Blois, J. L., ... Williams, J. W. (2012). Global climate  
852 evolution during the last deglaciation. *Proceedings of the National Academy of Sciences*,  
853 109(19), E1134. <https://doi.org/10.1073/pnas.1116619109>  
854
- 855 Dave, A. K., Courty, M.-A., Fitzsimmons, K. E., & Singhvi, A. K. (2019). Revisiting the  
856 contemporaneity of a mighty river and the Harappans: Archaeological, stratigraphic and  
857 chronometric constraints. *Quaternary Geochronology*, 49, 230–235. doi:  
858 10.1016/j.quageo.2018.05.002  
859
- 860 Ding, Z., Liu, T., Rutter, N. W., Yu, Z., Guo, Z., & Zhu, R. (1995). Ice-Volume Forcing of East Asian  
861 Winter Monsoon Variations in the Past 800,000 Years. *Quaternary Research*, 44(2), 149–159.  
862 Cambridge Core. doi: 10.1006/qres.1995.1059  
863
- 864 Ding, Z. L., Derbyshire, E., Yang, S. L., Yu, Z. W., Xiong, S. F., & Liu, T. S. (2002). Stacked 2.6-Ma  
865 grain size record from the Chinese loess based on five sections and correlation with the deep-  
866 sea  $\delta^{18}\text{O}$  record. *Paleoceanography*, 17(3), 5-1-5-21. doi:  
867 <https://doi.org/10.1029/2001PA000725>  
868
- 869 Duan, F., An, C., Wang, W., Herzschuh, U., Zhang, M., Zhang, H., Liu, Y., Zhao, Y., & Li, G. (2020).  
870 Dating of a late Quaternary loess section from the northern slope of the Tianshan Mountains  
871 (Xinjiang, China) and its paleoenvironmental significance. *Quaternary International*, 544, 104–  
872 112. <https://doi.org/10.1016/j.quaint.2020.02.034>  
873
- 874 Durcan, J. A., King, G. E., & Duller, G. A. T. (2015). DRAC: Dose Rate and Age Calculator for  
875 trapped charge dating. *Quaternary Geochronology*, 28, 54–61. doi:  
876 10.1016/j.quageo.2015.03.012  
877
- 878 Fenn, K., Durcan, J. A., Thomas, D. S. G., & Banak, A. (2020). A 180 ka record of environmental  
879 change at Erdut (Croatia): A new chronology for the loess–palaeosol sequence and its  
880 implications for environmental interpretation. *Journal of Quaternary Science*, 35(4), 582–593.  
881 doi: 10.1002/jqs.3201  
882
- 883 Fitzsimmons, K. E., Marković, S. B., & Hambach, U. (2012). Pleistocene environmental dynamics  
884 recorded in the loess of the middle and lower Danube basin. *Quaternary Science Reviews*, 41,  
885 104–118. doi: 10.1016/j.quascirev.2012.03.002  
886
- 887 Fitzsimmons, K. E., & Hambach, U. (2014). Loess accumulation during the last glacial maximum:  
888 Evidence from Urluia, southeastern Romania. *Quaternary International*, 334–335, 74–85. doi:  
889 10.1016/j.quaint.2013.08.005  
890





- 891 Fitzsimmons, K. E. (2017). Reconstructing palaeoenvironments on desert margins: New  
892 perspectives from Eurasian loess and Australian dry lake shorelines. *Quaternary Science*  
893 *Reviews*, 171, 1–19. doi: 10.1016/j.quascirev.2017.05.018  
894
- 895 Fitzsimmons, K. E., Iovita, R., Sprafke, T., Glantz, M., Talamo, S., Horton, K., Beeton, T., Alipova,  
896 S., Bekseitov, G., Ospanov, Y., Deom, J.-M., Sala, R., & Taimagambetov, Z. (2017). A  
897 chronological framework connecting the early Upper Palaeolithic across the Central Asian  
898 piedmont. *Journal of Human Evolution*, 113, 107–126.  
899 <https://doi.org/10.1016/j.jhevol.2017.07.006>  
900
- 901 Fitzsimmons, K. E., Sprafke, T., Zielhofer, C., Günter, C., Deom, J.-M., Sala, R., & Iovita, R. (2018).  
902 Loess accumulation in the Tian Shan piedmont: Implications for palaeoenvironmental change  
903 in arid Central Asia. *Quaternary International*, 469, 30–43. doi: 10.1016/j.quaint.2016.07.041  
904
- 905 Fitzsimmons, K. E., Nowatzki, M., Dave, A. K., & Harder, H. (2020). Intersections between wind  
906 regimes, topography and sediment supply: Perspectives from aeolian landforms in Central  
907 Asia. *Palaeogeography, Palaeoclimatology, Palaeoecology*, 540, 109531. doi:  
908 10.1016/j.palaeo.2019.109531  
909
- 910 Frechen, M., Schweitzer, U., & Zander, A. (1996). Improvements in sample preparation for the  
911 fine grain technique. *Ancient TL*, 14(2), 15–17.  
912
- 913 Galbraith, R. F., Roberts, R. G., Laslett, G. M., Yoshida, H., & Olley, J. M. (1999). Optical dating  
914 of single and multiple grains of quartz from Jinmium rock shelter, northern Australia: Part I,  
915 experimental design and statistical models. *Archaeometry*, 41(2), 339–364. Scopus. doi:  
916 10.1111/j.1475-4754.1999.tb00987.x  
917
- 918 Grützner, C., Walker, R. T., Abdrakhmatov, K. E., Mukambaev, A., Elliott, A. J., & Elliott, J. R.  
919 (2017). Active Tectonics Around Almaty and along the Zailisky Alatau Ranges. *Tectonics*,  
920 36(10), 2192–2226. doi: <https://doi.org/10.1002/2017TC004657>  
921
- 922 Guérin, G., Mercier, N., & Adamiec, G. (2011). Dose-rate conversion factors: Update. *Ancient*  
923 *TL*, 29(1), 5–8.  
924
- 925 Hao, Q., Wang, L., Oldfield, F., Peng, S., Qin, L., Song, Y., Xu, B., Qiao, Y., Bloemendal, J., & Guo,  
926 Z. (2012). Delayed build-up of Arctic ice sheets during 400,000-year minima in insolation  
927 variability. *Nature*, 490(7420), 393–396. <https://doi.org/10.1038/nature11493>  
928
- 929 Hong, B., Gasse, F., Uchida, M., Hong, Y., Leng, X., Shibata, Y., An, N., Zhu, Y., & Wang, Y. (2014).  
930 Increasing summer rainfall in arid eastern-Central Asia over the past 8500 years. *Scientific*  
931 *Reports*, 4. Scopus. <https://doi.org/10.1038/srep05279>



932

933 Jain, M., & Singhvi, Ashok. K. (2001). Limits to depletion of blue-green light stimulated  
934 luminescence in feldspars: Implications for quartz dating. *Radiation Measurements*, 33(6),  
935 883–892. doi: 10.1016/S1350-4487(01)00104-4

936

937 Jia, J., Liu, H., Gao, F., & Xia, D. (2018). Variations in the westerlies in Central Asia since 16 ka  
938 recorded by a loess section from the Tien Shan Mountains. *Palaeogeography*,  
939 *Palaeoclimatology, Palaeoecology*, 504, 156–161. doi: 10.1016/j.palaeo.2018.05.021

940

941 Kang, S., Wang, X., & Lu, Y. (2013). Quartz OSL chronology and dust accumulation rate changes  
942 since the Last Glacial at Weinan on the southeastern Chinese Loess Plateau: Quartz OSL  
943 chronology and dust accumulation rates, SE Chinese Loess Plateau. *Boreas*, 42, 815–829. doi:  
944 10.1111/bor.12005

945

946 Kang, S., Wang, X., Lu, Y., Liu, W., Song, Y., & Wang, N. (2015). A high-resolution quartz OSL  
947 chronology of the Taledo loess over the past ~30 ka and its implications for dust accumulation  
948 in the Ili Basin, Central Asia. *Quaternary Geochronology*, 30, 181–187. doi:  
949 10.1016/j.quageo.2015.04.006

950

951 Kang, S., Du, J., Wang, N., Dong, J., Wang, D., Wang, X., Qiang, X., & Song, Y. (2020). Early  
952 Holocene weakening and mid- to late Holocene strengthening of the East Asian winter  
953 monsoon. *Geology*, 48(11), 1043–1047. <https://doi.org/10.1130/G47621.1>

954

955 Kohfeld, K. E., & Harrison, S. P. (2000). How well can we simulate past climates? Evaluating the  
956 models using global palaeoenvironmental datasets. *Quaternary Science Reviews*, 19(1–5),  
957 321–346. doi: 10.1016/S0277-3791(99)00068-2

958

959 Kohfeld, K. E., & Harrison, S. P. (2003). Glacial-interglacial changes in dust deposition on the  
960 Chinese Loess Plateau. *Quaternary Science Reviews*, 22(18), 1859–1878. doi: 10.1016/S0277-  
961 3791(03)00166-5

962

963 Kok, J. F., Adebisi, A. A., Albani, S., Balkanski, Y., Checa-Garcia, R., Chin, M., Colarco, P. R.,  
964 Hamilton, D. S., Huang, Y., Ito, A., Klose, M., Li, L., Mahowald, N. M., Miller, R. L., Obiso, V.,  
965 Pérez García-Pando, C., Rocha-Lima, A., & Wan, J. S. (2021). Contribution of the world's main  
966 dust source regions to the global cycle of desert dust. *Atmospheric Chemistry and Physics*  
967 *Discussions*, 2021, 1–34. <https://doi.org/10.5194/acp-2021-4>

968

969 Konert, M., & Vandenberghe, J. (1997). Comparison of laser grain size analysis with pipette and  
970 sieve analysis: A solution for the underestimation of the clay fraction. *Sedimentology*, 44(3),  
971 523–535. doi: 10.1046/j.1365-3091.1997.d01-38.x

972



- 973 Kong, P., Fink, D., Na, C., & Huang, F. (2009). Late Quaternary glaciation of the Tianshan, Central  
974 Asia, using cosmogenic  $^{10}\text{Be}$  surface exposure dating. *Quaternary Research*, 72(2), 229–233.  
975 doi: 10.1016/j.yqres.2009.06.002  
976
- 977 Koppes, M., Gillespie, A. R., Burke, R. M., Thompson, S. C., & Stone, J. (2008). Late Quaternary  
978 glaciation in the Kyrgyz Tien Shan. *Quaternary Science Reviews*, 27(7), 846–866. doi:  
979 10.1016/j.quascirev.2008.01.009  
980
- 981 Kukla, G., Heller, F., Ming, L. X., Chun, X. T., Sheng, L. T., & Sheng, A. Z. (1988). Pleistocene  
982 climates in China dated by magnetic susceptibility. *Geology*, 16(9), 811–814. doi:  
983 10.1130/0091-7613(1988)016<0811:PCICDB>2.3.CO;2  
984
- 985 Lai, Z., Wintle, A. G., & Thomas, D. S. G. (2007). Rates of dust deposition between 50 ka and 20  
986 ka revealed by OSL dating at Yuanbao on the Chinese Loess Plateau. *Palaeogeography*,  
987 *Palaeoclimatology*, *Palaeoecology*, 248(3), 431–439. doi:  
988 <https://doi.org/10.1016/j.palaeo.2006.12.013>  
989
- 990 Lai, Z.-P., & Wintle, A. G. (2006). Locating the boundary between the Pleistocene and the  
991 Holocene in Chinese loess using luminescence. *The Holocene*, 16(6), 893–899. doi:  
992 10.1191/0959683606hol980rr  
993
- 994 Li, Yingkui, Liu, G., Kong, P., Harbor, J., Chen, Y., & Caffee, M. (2011). Cosmogenic nuclide  
995 constraints on glacial chronology in the source area of the Urumqi River, Tian Shan, China.  
996 *Journal of Quaternary Science*, 26(3), 297–304. doi: 10.1002/jqs.1454  
997
- 998 Li, Yingkui, Liu, G., Chen, Y., Li, Y., Harbor, J., Stroeve, A. P., Caffee, M., Zhang, M., Li, C., & Cui,  
999 Z. (2014). Timing and extent of Quaternary glaciations in the Tianger Range, eastern Tian Shan,  
1000 China, investigated using  $^{10}\text{Be}$  surface exposure dating. *Quaternary Science Reviews*, 98, 7–  
1001 23. <https://doi.org/10.1016/j.quascirev.2014.05.009>  
1002
- 1003 Li, G., Wen, L., Xia, D., Duan, Y., Rao, Z., Madsen, D. B., Wei, H., Li, F., Jia, J., & Chen, F. (2015).  
1004 Quartz OSL and K-feldspar pIRIR dating of a loess/paleosol sequence from arid central Asia,  
1005 Tianshan Mountains, NW China. *Quaternary Geochronology*, 28, 40–53. doi:  
1006 <https://doi.org/10.1016/j.quageo.2015.03.011>  
1007
- 1008 Li, Guoqiang, Rao, Z., Duan, Y., Xia, D., Wang, L., Madsen, D. B., Jia, J., Wei, H., Qiang, M., Chen,  
1009 J., & Chen, F. (2016)a. Paleoenvironmental changes recorded in a luminescence dated  
1010 loess/paleosol sequence from the Tianshan Mountains, arid central Asia, since the Penultimate  
1011 Glaciation. *Earth and Planetary Science Letters*, 448, 1–12.  
1012 <https://doi.org/10.1016/j.epsl.2016.05.008>  
1013



- 1014 Li, Yun, Song, Y., Lai, Z., Han, L., & An, Z. (2016)b. Rapid and cyclic dust accumulation during  
1015 MIS 2 in Central Asia inferred from loess OSL dating and grain-size analysis. *Scientific Reports*,  
1016 6(1), 32365. doi: 10.1038/srep32365  
1017
- 1018 Li, Guoqiang, Chen, F., Xia, D., Yang, H., Zhang, X., Madsen, D., Oldknow, C., Wei, H., Rao, Z., &  
1019 Qiang, M. (2018)a. A Tianshan Mountains loess-paleosol sequence indicates anti-phase  
1020 climatic variations in arid central Asia and in East Asia. *Earth and Planetary Science Letters*, 494,  
1021 153–163. <https://doi.org/10.1016/j.epsl.2018.04.052>  
1022
- 1023 Li, Yue, Song, Y., Fitzsimmons, K. E., Chen, X., Wang, Q., Sun, H., & Zhang, Z. (2018)b. New  
1024 evidence for the provenance and formation of loess deposits in the Ili River Basin, Arid Central  
1025 Asia. *Aeolian Research*, 35, 1–8. doi: <https://doi.org/10.1016/j.aeolia.2018.08.002>  
1026
- 1027 Li, Y., Song, Y., Fitzsimmons, K. E., Chang, H., Orozbaev, R., & Li, X. (2018)c. Eolian dust dispersal  
1028 patterns since the last glacial period in eastern Central Asia: Insights from a loess-paleosol  
1029 sequence in the Ili Basin. *Climate of the Past*, 14(3), 271–286. doi: 10.5194/cp-14-271-2018  
1030
- 1031 Li, Yue, Song, Y., Qiang, M., Miao, Y., & Zeng, M. (2019)a. Atmospheric Dust Variations in the Ili  
1032 Basin, Northwest China, During the Last Glacial Period as Revealed by a High Mountain Loess-  
1033 Paleosol Sequence. *Journal of Geophysical Research: Atmospheres*, 124(15), 8449–8466. doi:  
1034 10.1029/2019JD030470  
1035
- 1036 Li, Y., Song, Y., Yin, Q., Han, L., & Wang, Y. (2019)b. Orbital and millennial northern mid-latitude  
1037 westerlies over the last glacial period. *Climate Dynamics*, 53(5–6), 3315–3324. doi:  
1038 10.1007/s00382-019-04704-5  
1039
- 1040 Li, Guoqiang, Yang, H., Stevens, T., Zhang, X., Zhang, H., Wei, H., Zheng, W., Li, L., Liu, X., Chen,  
1041 J., Xia, D., Oldknow, C., Ye, W., & Chen, F. (2020). Differential ice volume and orbital modulation  
1042 of Quaternary moisture patterns between Central and East Asia. *Earth and Planetary Science*  
1043 *Letters*, 530, 115901. doi: <https://doi.org/10.1016/j.epsl.2019.115901>  
1044
- 1045 Licht, A., Dupont-Nivet, G., Pullen, A., Kapp, P., Abels, H. A., Lai, Z., Guo, Z., Abell, J., & Giesler,  
1046 D. (2016). Resilience of the Asian atmospheric circulation shown by Paleogene dust  
1047 provenance. *Nature Communications*, 7(1), 12390. <https://doi.org/10.1038/ncomms12390>  
1048
- 1049 Lifton, N., Beel, C., Hätteland, C., Kassab, C., Rogozhina, I., Heermance, R., ... Stroeven, A. P.  
1050 (2014). Constraints on the late Quaternary glacial history of the Inylchek and Sary-Dzaz valleys  
1051 from in situ cosmogenic  $^{10}\text{Be}$  and  $^{26}\text{Al}$ , eastern Kyrgyz Tian Shan. *Quaternary Science Reviews*,  
1052 101, 77–90. doi: 10.1016/j.quascirev.2014.06.032  
1053



- 1054 Lisiecki, L. E., & Raymo, M. E. (2005). A Pliocene-Pleistocene stack of 57 globally distributed  
1055 benthic  $\delta^{18}\text{O}$  records. *Paleoceanography*, 20(1). doi: 10.1029/2004PA001071  
1056
- 1057 Liu, T. (1962). The huangtu (loess) of China. *Acta Geol. Sinica*, 42, 1–14.  
1058
- 1059 Liu, T. S. (1985). *Loess and Environment*. China Ocean Press (Beijing).  
1060
- 1061 Liu, T., & Ding, Z. (1998). Chinese loess and the paleomonsoon. *Annual Review of Earth and*  
1062 *Planetary Sciences*, 26(1), 111–145. doi: 10.1146/annurev.earth.26.1.111  
1063
- 1064 Liu, Y., Liu, X., Ma, L., Kang, S., Qiang, X., Guo, F., & Sun, Y. (2020). Temporal–spatial variations  
1065 in aeolian flux on the Chinese Loess Plateau during the last 150 ka. *Geological Magazine*,  
1066 157(5), 757–767. doi: 10.1017/S0016756819001067  
1067
- 1068 Łomotowski, J., Burszta-Adamiak, E., Kęszycka, M., Jary, Z. (2008). In: *Metody i techniki*  
1069 *optyczne w badaniach zawiesin*, *Badania Sy.* Instytut Badań Systemowych PAN, Warszawa.  
1070 (n.d.).  
1071
- 1072 Lu, H., & Sun, D. (2000). Pathways of dust input to the Chinese Loess Plateau during the last  
1073 glacial and interglacial periods. *Catena*, 40(3), 251–261. doi: 10.1016/S0341-8162(00)00090-4  
1074
- 1075 Lu, Y. C., Wang, X. L., & Wintle, A. G. (2007). A new OSL chronology for dust accumulation in  
1076 the last 130,000 yr for the Chinese Loess Plateau. *Quaternary Research*, 67(1), 152–160. doi:  
1077 10.1016/j.yqres.2006.08.003  
1078
- 1079 Lydolph, P. E. (1977). *Climates of the Soviet Union*. Amsterdam; New York: Elsevier Scientific  
1080 Pub. Co.  
1081
- 1082 Machalett, B., Frechen, M., Hambach, U., Oches, E. A., Zöller, L., & Marković, S. B. (2006). The  
1083 loess sequence from Remisowka (northern boundary of the Tien Shan Mountains,  
1084 Kazakhstan)—Part I: Luminescence dating. *Quaternary International*, 152–153, 192–201. doi:  
1085 10.1016/j.quaint.2005.12.014  
1086
- 1087 Machalett, Björn, Oches, E. A., Frechen, M., Zöller, L., Hambach, U., Mavlyanova, N. G., ...  
1088 Endlicher, W. (2008). Aeolian dust dynamics in central Asia during the Pleistocene: Driven by  
1089 the long-term migration, seasonality, and permanency of the Asiatic polar front: Aeolian dust  
1090 dynamics in Central Asia. *Geochemistry, Geophysics, Geosystems*, 9(8), n/a–n/a. doi:  
1091 10.1029/2007GC001938  
1092
- 1093 Maher, B. A. (2016). Palaeoclimatic records of the loess/palaeosol sequences of the Chinese  
1094 Loess Plateau. *Quaternary Science Reviews*, 154, 23–84. doi: 10.1016/j.quascirev.2016.08.004



1095

1096 Marković, S. B., Stevens, T., Kukla, G. J., Hambach, U., Fitzsimmons, K. E., Gibbard, P., ... Svirčev,  
1097 Z. (2015). Danube loess stratigraphy—Towards a pan-European loess stratigraphic model.  
1098 *Earth-Science Reviews*, 148, 228–258. doi: 10.1016/j.earscirev.2015.06.005

1099

1100 Martin, J. H. (1990). Glacial-interglacial CO<sub>2</sub> change: The Iron Hypothesis. *Paleoceanography*,  
1101 5(1), 1–13. doi: 10.1029/PA005i001p00001

1102

1103 Martínez-García, A., Sigman, D. M., Ren, H., Anderson, R. F., Straub, M., Hodell, D. A., ... Haug,  
1104 G. H. (2014). Iron Fertilization of the Subantarctic Ocean During the Last Ice Age. *Science*,  
1105 343(6177), 1347. doi: 10.1126/science.1246848

1106

1107 Muhs, D. R. (2007). Loess deposits, origins and properties. In *Encyclopedia of Quaternary*  
1108 *Science* (pp. 1405–1418). Elsevier. doi: 10.1016/B0-44-452747-8/00158-7

1109

1110 Murray, A. S., & Wintle, A. G. (2000). Luminescence dating of quartz using an improved single-  
1111 aliquot regenerative-dose protocol. *Radiation Measurements*, 32(1), 57–73. doi:  
1112 [https://doi.org/10.1016/S1350-4487\(99\)00253-X](https://doi.org/10.1016/S1350-4487(99)00253-X)

1113

1114 Murray, A. S., & Wintle, A. G. (2003). The single aliquot regenerative dose protocol: Potential  
1115 for improvements in reliability. *Radiation Measurements*, 37(4), 377–381. doi:  
1116 [https://doi.org/10.1016/S1350-4487\(03\)00053-2](https://doi.org/10.1016/S1350-4487(03)00053-2)

1117

1118 Narisma, G. T., Foley, J. A., Licker, R., & Ramankutty, N. (2007). Abrupt changes in rainfall during  
1119 the twentieth century. *Geophysical Research Letters*, 34(6). doi:  
1120 <https://doi.org/10.1029/2006GL028628>

1121

1122 Nie, J., Stevens, T., Rittner, M., Stockli, D., Garzanti, E., Limonta, M., Bird, A., Andò, S.,  
1123 Vermeesch, P., Saylor, J., Lu, H., Breecker, D., Hu, X., Liu, S., Resentini, A., Vezzoli, G., Peng, W.,  
1124 Carter, A., Ji, S., & Pan, B. (2015). Loess Plateau storage of Northeastern Tibetan Plateau-  
1125 derived Yellow River sediment. *Nature Communications*, 6(1), 8511.  
1126 <https://doi.org/10.1038/ncomms9511>

1127

1128 Nie, J., Pullen, A., Garzzone, C. N., Peng, W., & Wang, Z. (2018). Pre-Quaternary decoupling  
1129 between Asian aridification and high dust accumulation rates. *Science Advances*, 4(2),  
1130 eaao6977. doi: 10.1126/sciadv.aao6977

1131

1132 Obruchev, V. A. (1945). Loess types and their origin. *American Journal of Science*, 243(5), 256–  
1133 262. doi: 10.2475/ajs.243.5.256

1134



- 1135 Owen, Lewis A., Finkel, R. C., Haizhou, M., Spencer, J. Q., Derbyshire, E., Barnard, P. L., & Caffee,  
1136 M. W. (2003)a. Timing and style of Late Quaternary glaciation in northeastern Tibet. *Geological*  
1137 *Society of America Bulletin*, 115(11), 1356. doi: 10.1130/B25314.1  
1138
- 1139 Owen, L.A., Ma, H., Derbyshire, E., Spencer, J. Q., Barnard, P. L., Zeng, Y. N., ... Caffee, M. W.  
1140 (2003)b. The timing and style of Late Quaternary glaciation in the La Ji Mountains, NE Tibet:  
1141 Evidence for restricted glaciation during the latter part of the Last Glacial. *Zeitschrift Fur*  
1142 *Geomorphologie, Supplementband*, 130, 263–276.  
1143
- 1144 Owen, L.A., Finkel, R. C., Haizhou, M., & Barnard, P. L. (2006). Late Quaternary landscape  
1145 evolution in the Kunlun Mountains and Qaidam Basin, Northern Tibet: A framework for  
1146 examining the links between glaciation, lake level changes and alluvial fan formation.  
1147 *Quaternary International*, 154–155, 73–86. Scopus. doi: 10.1016/j.quaint.2006.02.008  
1148
- 1149 Owen, Lewis A., & Dortch, J. M. (2014). Nature and timing of Quaternary glaciation in the  
1150 Himalayan–Tibetan orogen. *Quaternary Science Reviews*, 88, 14–54. doi:  
1151 10.1016/j.quascirev.2013.11.016  
1152
- 1153 Pécsi, M. (1990). Loess is not just the accumulation of dust. *Quaternary International*, 7–8, 1–  
1154 21. doi: [https://doi.org/10.1016/1040-6182\(90\)90034-2](https://doi.org/10.1016/1040-6182(90)90034-2)  
1155
- 1156 Porter, S. C., & An, Z. (1995). Correlation between climate events in the North Atlantic and  
1157 China during the last glaciation. *Nature*, 375(6529), 305–308. doi: 10.1038/375305a0  
1158
- 1159 Prescott, J. R., & Hutton, J. T. (1994). Cosmic ray contributions to dose rates for luminescence  
1160 and ESR dating: Large depths and long-term time variations. *Radiation Measurements*, 23(2),  
1161 497–500. doi: 10.1016/1350-4487(94)90086-8  
1162
- 1163 Pye, K. (1987). *Aeolian Dust and Dust Deposits*. Academic Press, London.  
1164
- 1165 Qiu, F., & Zhou, L. (2015). A new luminescence chronology for the Mangshan loess-palaeosol  
1166 sequence on the southern bank of the Yellow River in Henan, central China. *Quaternary*  
1167 *Geochronology*, 30, 24–33. doi: 10.1016/j.quageo.2015.06.014  
1168
- 1169 Ran, M., & Feng, Z. (2013). Holocene moisture variations across China and driving mechanisms:  
1170 A synthesis of climatic records. *Quaternary International*, 313–314, 179–193. doi:  
1171 10.1016/j.quaint.2013.09.034  
1172
- 1173 Rasmussen, S. O., Bigler, M., Blockley, S. P., Blunier, T., Buchardt, S. L., Clausen, H. B., ...  
1174 Winstrup, M. (2014). A stratigraphic framework for abrupt climatic changes during the Last  
1175 Glacial period based on three synchronized Greenland ice-core records: Refining and extending





- 1176 the INTIMATE event stratigraphy. *Quaternary Science Reviews*, 106, 14–28. doi:  
1177 10.1016/j.quascirev.2014.09.007  
1178
- 1179 Rother, H., Stauch, G., Loibl, D., Lehmkuhl, F., & Freeman, S. P. H. T. (2017). Late Pleistocene  
1180 glaciations at Lake Donggi Cona, eastern Kunlun Shan (NE Tibet): Early maxima and a  
1181 diminishing trend of glaciation during the last glacial cycle. *Boreas*, 46(3), 503–524. doi:  
1182 10.1111/bor.12227  
1183
- 1184 Ruth, U., Bigler, M., Röthlisberger, R., Siggaard-Andersen, M.-L., Kipfstuhl, S., Goto-Azuma, K.,  
1185 ... Steffensen, J. P. (2007). Ice core evidence for a very tight link between North Atlantic and  
1186 east Asian glacial climate. *Geophysical Research Letters*, 34(3). doi: 10.1029/2006GL027876  
1187
- 1188 Schaetzl, R. J., Bettis, E. A., Crouvi, O., Fitzsimmons, K. E., Grimley, D. A., Hambach, U., ... Zech,  
1189 R. (2018). Approaches and challenges to the study of loess—Introduction to the LoessFest  
1190 Special Issue. *Quaternary Research* 89 (3), 563–618. doi: 10.1017/qua.2018.15  
1191
- 1192 Schaffernicht, E. J., Ludwig, P., & Shao, Y. (2020). Linkage between dust cycle and loess of the  
1193 Last Glacial Maximum in Europe. *Atmospheric Chemistry and Physics*, 20(8), 4969–4986. doi:  
1194 10.5194/acp-20-4969-2020  
1195
- 1196 Schulte, P., Sprafke, T., Rodrigues, L., & Fitzsimmons, K. E. (2018). Are fixed grain size ratios  
1197 useful proxies for loess sedimentation dynamics? Experiences from Remizovka, Kazakhstan.  
1198 *Aeolian Research*, 31(B), 131–140. doi: 10.1016/j.aeolia.2017.09.002  
1199
- 1200 Schurr, B., Ratschbacher, L., Sippl, C., Gloaguen, R., Yuan, X., & Mechie, J. (2014).  
1201 Seismotectonics of the Pamir. *Tectonics*, 33(8), 1501–1518. doi: 10.1002/2014TC003576  
1202
- 1203 Selander, J., Oskin, M., Ormukov, C., & Abdrakhmatov, K. (2012). Inherited strike-slip faults as  
1204 an origin for basement-cored uplifts: Example of the Kungey and Zailiskey ranges, northern  
1205 Tian Shan. *Tectonics*, 31(4). doi: <https://doi.org/10.1029/2011TC003002>  
1206
- 1207 Singhvi, A. K., Bluszcz, A., Bateman, M. D., & Rao, M. S. (2001). Luminescence dating of loess–  
1208 palaeosol sequences and coversands: Methodological aspects and palaeoclimatic implications.  
1209 *Recent Research on Loess and Palaeosols, Pure and Applied*, 54(1), 193–211. doi:  
1210 10.1016/S0012-8252(01)00048-4  
1211
- 1212 Smalley, I. (1995). Making the material: The formation of silt sized primary mineral particles for  
1213 loess deposits. *Quaternary Science Reviews*, 14(7), 645–651. doi:  
1214 [https://doi.org/10.1016/0277-3791\(95\)00046-1](https://doi.org/10.1016/0277-3791(95)00046-1)  
1215



- 1216 Smalley, I. J., Kumar, R., O'Hara Dhand, K., Jefferson, I. F., & Evans, R. D. (2005). The formation  
1217 of silt material for terrestrial sediments: Particularly loess and dust. *Sedimentary Geology*,  
1218 179(3), 321–328. doi: 10.1016/j.sedgeo.2005.06.011  
1219
- 1220 Smalley, I., O'Hara-Dhand, K., & Kwong, J. (2014). China: Materials for a loess landscape.  
1221 *Catena*, 117, 100–107. doi: 10.1016/j.catena.2013.11.016  
1222
- 1223 Song, Yougui, Li, C., Zhao, J., Cheng, P., & Zeng, M. (2012). A combined luminescence and  
1224 radiocarbon dating study of the Ili loess, Central Asia. *Quaternary Geochronology*, 10, 2–7. doi:  
1225 10.1016/j.quageo.2012.04.005  
1226
- 1227 Song, Yougui, Chen, X., Qian, L., Li, C., Li, Y., Li, X., ... An, Z. (2014). Distribution and composition  
1228 of loess sediments in the Ili Basin, Central Asia. *Quaternary International*, 334–335, 61–73. doi:  
1229 10.1016/j.quaint.2013.12.053  
1230
- 1231 Song, Yougui, Lai, Z., Li, Y., Chen, T., & Wang, Y. (2015). Comparison between luminescence  
1232 and radiocarbon dating of late Quaternary loess from the Ili Basin in Central Asia. *Quaternary*  
1233 *Geochronology*, 30, 405–410. doi: 10.1016/j.quageo.2015.01.012  
1234
- 1235 Sprafke, T., Fitzsimmons, K. E., Grützner, C., Elliot, A., Marquer, L., & Nigmatova, S. (2018).  
1236 Reevaluation of Late Pleistocene loess profiles at Remizovka (Kazakhstan) indicates the  
1237 significance of topography in evaluating terrestrial paleoclimate records. *Quaternary Research*,  
1238 89(3), 674–690. doi: 10.1017/qua.2017.103  
1239
- 1240 Stevens, Thomas, Armitage, S. J., Lu, H., & Thomas, D. S. G. (2006). Sedimentation and  
1241 diagenesis of Chinese loess: Implications for the preservation of continuous, high-resolution  
1242 climate records. *Geology*, 34(10), 849–852. doi: 10.1130/G22472.1  
1243
- 1244 Stevens, Thomas, Thomas, D. S. G., Armitage, S. J., Lunn, H. R., & Lu, H. (2007). Reinterpreting  
1245 climate proxy records from late Quaternary Chinese loess: A detailed OSL investigation. *Earth-*  
1246 *Science Reviews*, 80(1), 111–136. doi: <https://doi.org/10.1016/j.earscirev.2006.09.001>  
1247
- 1248 Stevens, Thomas, Lu, H., Thomas, D. S. G., & Armitage, S. J. (2008). Optical dating of abrupt  
1249 shifts in the late Pleistocene East Asian monsoon. *Geology*, 36(5), 415. doi: 10.1130/G24524A.1  
1250
- 1251 Stevens, T., Carter, A., Watson, T. P., Vermeesch, P., Andò, S., Bird, A. F., Lu, H., Garzanti, E.,  
1252 Cottam, M. A., & Sevastjanova, I. (2013). Genetic linkage between the Yellow River, the Mu Us  
1253 desert and the Chinese Loess Plateau. *Quaternary Science Reviews*, 78, 355–368.  
1254 <https://doi.org/10.1016/j.quascirev.2012.11.032>  
1255



- 1256 Stevens, Thomas, Buylaert, J.-P., Lu, H., Thiel, C., Murray, A., Frechen, M., Yi, S., & Zeng, L.  
1257 (2016). Mass accumulation rate and monsoon records from Xifeng, Chinese Loess Plateau,  
1258 based on a luminescence age model: Monsoon records from Chinese Loess Plateau. *Journal of*  
1259 *Quaternary Science*, 31(4), 391–405. <https://doi.org/10.1002/jqs.2848>  
1260
- 1261 Stevens, T., Buylaert, J.-P., Thiel, C., Újvári, G., Yi, S., Murray, A. S., ... Lu, H. (2018). Ice-volume-  
1262 forced erosion of the Chinese Loess Plateau global Quaternary stratotype site. *Nature*  
1263 *Communications*, 9(1), 983. doi: 10.1038/s41467-018-03329-2  
1264
- 1265 Stevens, T. (2019). Applications in loessic environments. In *Handbook of Luminescence Dating*.  
1266 Ed. M. Bateman and I. Bailiff. Caithness, Whittles Publishing, 153-190.  
1267
- 1268 Stoops, G. (2003). *Guidelines for Analysis and Description of Soil and Regolith Thin Sections*.  
1269 Soil Science Society of America, Madison, Wisconsin, 184 p.  
1270
- 1271 Sun, J. (2002). Source Regions and Formation of the Loess Sediments on the High Mountain  
1272 Regions of Northwestern China. *Quaternary Research*, 58(3), 341–351. doi:  
1273 <https://doi.org/10.1006/qres.2002.2381>  
1274
- 1275 Sun, J., & Liu, T. (2000). Stratigraphic Evidence for the Uplift of the Tibetan Plateau between  
1276 ~1.1 and ~0.9 myr Ago. *Quaternary Research*, 54(3), 309–320. doi:  
1277 <https://doi.org/10.1006/qres.2000.2170>  
1278
- 1279 Sun, Y., & An, Z. (2005). Late Pliocene-Pleistocene changes in mass accumulation rates of eolian  
1280 deposits on the central Chinese Loess Plateau. *Journal of Geophysical Research*, 110(D23),  
1281 D23101. doi: 10.1029/2005JD006064  
1282
- 1283 Sun, Y., Clemens, S. C., Morrill, C., Lin, X., Wang, X., & An, Z. (2012). Influence of Atlantic  
1284 meridional overturning circulation on the East Asian winter monsoon. *Nature Geoscience*, 5(1),  
1285 46–49. doi: 10.1038/ngeo1326  
1286
- 1287 Thiel, C., Buylaert, J.-P., Murray, A., Terhorst, B., Hofer, I., Tsukamoto, S., & Frechen, M. (2011).  
1288 Luminescence dating of the Stratzing loess profile (Austria) – Testing the potential of an  
1289 elevated temperature post-IR IRSI protocol. *Quaternary International*, 234(1), 23–31. doi:  
1290 <https://doi.org/10.1016/j.quaint.2010.05.018>  
1291
- 1292 Timar, A., Vandenberghe, D., Panaiotu, E. C., Panaiotu, C. G., Necula, C., Cosma, C., & van den  
1293 haute, P. (2010). Optical dating of Romanian loess using fine-grained quartz. *Quaternary*  
1294 *Geochronology*, 5(2), 143–148. doi: 10.1016/j.quageo.2009.03.003  
1295



- 1296 Timar-Gabor, A., Buylaert, J.-P., Guralnik, B., Trandafir-Antohi, O., Constantin, D., Anechitei-  
1297 Deacu, V., Jain, M., Murray, A. S., Porat, N., Hao, Q., & Wintle, A. G. (2017). On the importance  
1298 of grain size in luminescence dating using quartz. *Radiation Measurements*, 106, 464–471.  
1299 <https://doi.org/10.1016/j.radmeas.2017.01.009>  
1300
- 1301 Újvári, G., Kovács, J., Varga, G., Raucsik, B., & Marković, S. B. (2010). Dust flux estimates for the  
1302 Last Glacial Period in East Central Europe based on terrestrial records of loess deposits: A  
1303 review. *Quaternary Science Reviews*, 29(23), 3157–3166. doi:  
1304 10.1016/j.quascirev.2010.07.005  
1305
- 1306 Vandenberghe, J. (2013). Grain size of fine-grained windblown sediment: A powerful proxy for  
1307 process identification. *Earth-Science Reviews*, 121, 18–30. doi:  
1308 10.1016/j.earscirev.2013.03.001  
1309
- 1310 Vriend, M., Prins, M. A., Buylaert, J.-P., Vandenberghe, J., & Lu, H. (2011). Contrasting dust  
1311 supply patterns across the north-western Chinese Loess Plateau during the last glacial-  
1312 interglacial cycle. *Quaternary International*, 240(1), 167–180. doi:  
1313 <https://doi.org/10.1016/j.quaint.2010.11.009>  
1314
- 1315 Wang, L., Jia, J., Xia, D., Liu, H., Gao, F., Duan, Y., Wang, Q., Xie, H., & Chen, F. (2019)a. Climate  
1316 change in arid central Asia since MIS 2 revealed from a loess sequence in Yili Basin, Xinjiang,  
1317 China. *Quaternary International*, 502, 258–266. <https://doi.org/10.1016/j.quaint.2018.02.032>  
1318
- 1319 Wang, L., Jia, J., Zhao, H., Liu, H., Duan, Y., Xie, H., Zhang, D. D., & Chen, F. (2019)b. Optical  
1320 dating of Holocene paleosol development and climate changes in the Yili Basin, arid central  
1321 Asia. *The Holocene*, 29(6), 1068–1077. <https://doi.org/10.1177/0959683619831432>  
1322
- 1323 Wintle, A. G., & Murray, A. S. (2006). A review of quartz optically stimulated luminescence  
1324 characteristics and their relevance in single-aliquot regeneration dating protocols. *Radiation*  
1325 *Measurements*, 41(4), 369–391. doi: 10.1016/j.radmeas.2005.11.001  
1326
- 1327 Wyrwoll, K.-H., Wei, J., Lin, Z., Shao, Y., & He, F. (2016). Cold surges and dust events:  
1328 Establishing the link between the East Asian Winter Monsoon and the Chinese loess record.  
1329 *Quaternary Science Reviews*, 149, 102–108. doi:  
1330 <https://doi.org/10.1016/j.quascirev.2016.04.015>  
1331
- 1332 Xu, Z., Stevens, T., Yi, S., Mason, J. A., & Lu, H. (2018). Seesaw pattern in dust accumulation on  
1333 the Chinese Loess Plateau forced by late glacial shifts in the East Asian monsoon. *Geology*,  
1334 46(10), 871–874. doi: 10.1130/G45105.1  
1335



- 1336 Yang, S., & Ding, Z. (2010). Drastic climatic shift at ~2.8Ma as recorded in eolian deposits of  
1337 China and its implications for redefining the Pliocene-Pleistocene boundary. *Plio-Pleistocene*  
1338 *Correlation and Global Change*, 219(1), 37–44. doi: 10.1016/j.quaint.2009.10.029  
1339
- 1340 Yang, S., Ding, Z., Li, Y., Wang, X., Jiang, W., & Huang, X. (2015). Warming-induced  
1341 northwestward migration of the East Asian monsoon rain belt from the Last Glacial Maximum  
1342 to the mid-Holocene. *Proceedings of the National Academy of Sciences*, 112(43), 13178. doi:  
1343 10.1073/pnas.1504688112  
1344
- 1345 Yang, H., Li, G., Huang, X., Wang, X., Zhang, Y., Jonell, T. N., Jin, M., Chen, C., Zhao, W., Zhang,  
1346 H., Wang, Z., & Deng, Y. (2020). Loess depositional dynamics and paleoclimatic changes in the  
1347 Yili Basin, Central Asia, over the past 250 ka. *Catena*, 195, 104881.  
1348 <https://doi.org/10.1016/j.catena.2020.104881>  
1349
- 1350 Youn, J. H., Seong, Y. B., Choi, J. H., Abdrakhmatov, K., & Ormukov, C. (2014). Loess deposits in  
1351 the northern Kyrgyz Tien Shan: Implications for the paleoclimate reconstruction during the Late  
1352 Quaternary. *Catena*, 117, 81–93. doi: <https://doi.org/10.1016/j.catena.2013.09.007>  
1353